# DOUBLE HOPF BIFURCATIONS IN THE DIFFERENTIALLY HEATED ROTATING ANNULUS*

GREGORY M. LEWIS† AND WAYNE NAGATA‡

**Abstract.** We study a mathematical model of the differentially heated rotating fluid annulus experiment. In particular, we analyze the double Hopf bifurcations that occur along the transition between axisymmetric steady solutions and non-axisymmetric rotating waves. The model uses the Navier-Stokes equations in the Boussinesq approximation. At the bifurcation points, center manifold reduction and normal form theory are used to deduce the local behaviour of the full system of partial differential equations from a low-dimensional system of ordinary differential equations.

It is not possible to compute the relevant eigenvalues and eigenfunctions analytically. Therefore, the linear part of the equations is discretized and the eigenvalues and eigenfunctions are approximated from the resulting matrix eigenvalue problem. However, the projection onto the center manifold and reduction to normal form can be done analytically. Thus, a combination of analytical and numerical methods are used to obtain numerical approximations of the normal form coefficients, from which the dynamics are deduced.

The results indicate that, close to the transition, there are regions in parameter space where there are multiple stable waves. Hysteresis of these waves is predicted. The validity of the results is shown by their consistency with experimental observations.

**Key words.** differentially heated rotating fluid experiment, axisymmetric to non-axisymmetric transition, hysteresis of rotating waves, center manifold reduction, numerical approximation of normal form coefficients

**AMS subject classifications.** 37N10, 76U05, 37N99

## 1. Introduction.

Laboratory experiments that isolate the effects of differential heating and rotation have long been regarded as useful tools for studying the behaviour of large scale geophysical fluids, such as the atmosphere. The dynamic similarity of the various experiments and actual geophysical flows indicates that the form of the differential heating, the geometry of the system, the properties of the fluid, and the boundary conditions play a secondary role [13]. This is evidence that the character of large scale geophysical fluid flows is determined, to a large extent, by the differential heating and rotation. Consequently, an investigation of a mathematical model of a laboratory experiment itself can provide insight into the dynamical properties of large scale geophysical fluids. Furthermore, models of the experiments can be tractable, and the model and the method of analysis can be quantitatively validated *via* comparison with experimental observations. In constrast, a quantitative validation is not possible when studying direct, simplified models of large scale flows.

We study a model of a particular laboratory experiment in which the changes in the flow patterns in a differentially heated rotating annulus are observed as the imposed temperature gradient and rate of rotation are varied. We use an accurate mathematical model that is able to quantitatively reproduce some of the experimental observations [18], [19]. In the laboratory experiments, for small differential heating and rotation, a steady axisymmetric pattern is observed, *i.e.* the pattern is invariant under rotation. As the parameter values are increased, this relatively simple pattern

---

*This research was supported in part by the National Science and Engineering Research Council of Canada

†Department of Mathematics, University of British Columbia, Canada. Present address: The Fields Institute, 222 College St., Toronto, ON, M5T 3J1, Canada. This author was supported in part by a fellowship from the Killam Trusts. (`glewis@fields.utoronto.ca`).

‡Department of Mathematics, University of British Columbia, Canada. (`nagata@math.ubc.ca`)

becomes unstable and a wave motion appears. It is this transition from axisymmetric to non-axisymmetric flow that is of interest here.

We study the transition by directly analyzing the partial differential equations (PDEs) that describe the fluid flow in the rotating annulus. In particular, we study the double Hopf bifurcations that are found at isolated points along the transition. These double Hopf bifurcation points occur when the linearization about the steady axisymmetric solution has two pairs of complex conjugate eigenvalues that simultaneously cross the imaginary axis as the parameters are varied. Center manifold reduction is used to find the dynamics of the partial differential equations close to the bifurcation point. This is a method of simplifying the equations in a way that takes into account all the nonlinear interactions. The results are valid for parameter values close to the bifurcation point and when the bifurcating solutions are, in some sense, small. This method is sometimes referred to as weakly nonlinear analysis, because the nonlinear terms in the equations are assumed to be small but not negligible. Essentially, the technique is able to show the existence and stability of the bifurcating solutions, and give a first-order estimate of the solution itself, but it is not able to determine if the solution persists for values of the parameters far from the bifurcation point.

This type of bifurcation analysis has been successful in other applications to fluid flow. One of the best known is the onset of motion in a layer of fluid heated from below, Rayleigh-Bénard convection (see *e.g.* [24]). Another application of note is the Couette-Taylor problem (see [1] and the references contained therein), which is a fluid annulus experiment (without differential heating) where the inner and outer cylinders rotate at different rates, generating a shear flow in the fluid. A rich variety of behaviour has been found by experiment, some of which can be explained with bifurcation theory. In addition, bifurcation analysis has made several predictions of flow patterns that were subsequently confirmed by experimental results. In the geophysical fluid dynamics literature, an asymptotic method, formally equivalent to center manifold reduction, was used to analyze 'weakly nonlinear' wave-wave interactions (double Hopf bifurcations) in the two layer quasi-geostrophic potential vorticity equations in [20], [21], and [25] (see also [2] and [10]). The results indicated multiple stable wave solutions and hysteresis of these solutions. For all of these models, it is possible to find the results analytically.

In the field of geophysical fluid dynamics, few models exist that can be studied purely analytically. Since the model we study does not fall into this category, we use an analytical–numerical hybrid analysis technique. Using center manifold reduction, it is possible to analytically reduce the time-dependent nonlinear PDEs to a series of steady linear PDE problems. These linear systems are then solved numerically, which results in numerical approximations for the coefficients of the normal form equations, from which the local dynamics can be deduced. Not only are the linear problems less difficult to numerically approximate, but also the validity of the approximations is more easily verified. Thus, although numerical approximations must be made, this method of analysis gives evidence that the predicted dynamics corresponds to those of the PDEs. Essentially equivalent methods are used in the Couette-Taylor problem [1] and in [7], where a double Hopf bifurcation was analyzed in a barotropic quasi-geostrophic model. It should be noted that although similar methods were used in these problems, the numerics are substantially less intensive than those presented here. In fact, until recently, the numerics of this work would not have been possible on a personal computer.

In the next section, we describe the experiments in more detail. We discuss some general experimental results, and in so doing, introduce some of the flow features that our model reproduces. In Section 3, the dynamical equations are written explicitly. The methods of analysis are discussed in the following two sections, where the analytical methods are presented in Section 4 and the numerical methods are presented in Section 5. In Section 6, the results are described and discussed. A conclusion follows.

**2. Experimental Observations.** Many different experiments have been performed in an attempt to develop an understanding of differentially heated rotating fluid systems (see *e.g.* [13], [15], and [5]). The experiments often take the form of studying fluid flow in a rotating cylindrical annulus, where the differential heating is obtained by maintaining the inner and outer walls of the annulus at different temperatures. See Figure 2.1. The experiments consist of finding the various stable flow patterns that occur at different values of the rotation rate and differential heating. The results are typically given in a diagram where the transitions between the different flow types are plotted in parameter space, in terms of the Taylor number $\mathcal{T}$, and the thermal Rossby number $\mathcal{R}$ [4], [13]. The Taylor number

$$\mathcal{T} = \frac{4\Omega^2 R^4}{\nu^2}$$

is a dimensionless parameter measuring the relative importance of rotation to viscosity, where $\Omega$ is the rate of rotation, $R$ is the gap width of the annulus and $\nu$ is the kinematic viscosity of the fluid. The thermal Rossby number

$$\mathcal{R} = \frac{\alpha g D \Delta T}{\Omega^2 R^2}$$

is another dimensionless parameter measuring the relative importance of rotation to the differential heating, where $\Delta T$ is the difference in temperature between the inner and outer walls of the annulus, $\alpha$ is the coefficient of thermal expansion of the fluid, $D$ is the depth, and $g$ is the gravitational acceleration. If all other parameters are held fixed, there is a one-to-one relationship between these two dimensionless parameters and the two physical parameters that are varied during experiments: the differential heating $\Delta T$ and rate of rotation $\Omega$.

Most of the experiments find four main flow regimes in different regions of parameter space (see Figure 2.2): (1) **Axisymmetric Flow**; this flow is characterized by its azimuthal invariance. (2) **Steady Waves**; the flow in this region is non-axisymmetric and resembles a rotating wave with constant amplitude and phase. Different wavelengths are seen in different subregions, with the possibility of observing stable waves of different wavelengths within the same subregion. The transitions between the subregions exhibit hysteresis. (3) **Vacillation**; in this region, the amplitude or structure of the observed wave varies apparently periodically in time. (4) **Irregular Flow**; this region is characterized by its irregular nature in both space and time.

All of the observed flows have their counterparts in the Earth's atmosphere [6],[13]. The axisymmetric flow resembles the Hadley cell, which is observed in the atmosphere near the equator where the 'local' rotation rate and differential heating are relatively small. In mid-latitude regions of the Earth, the flow sometimes has wave characteristics that resemble the steady waves and vacillations seen in the experiments. Here, in both the atmosphere and experiments, the flow trajectories are curved and vertical motion is inhibited.

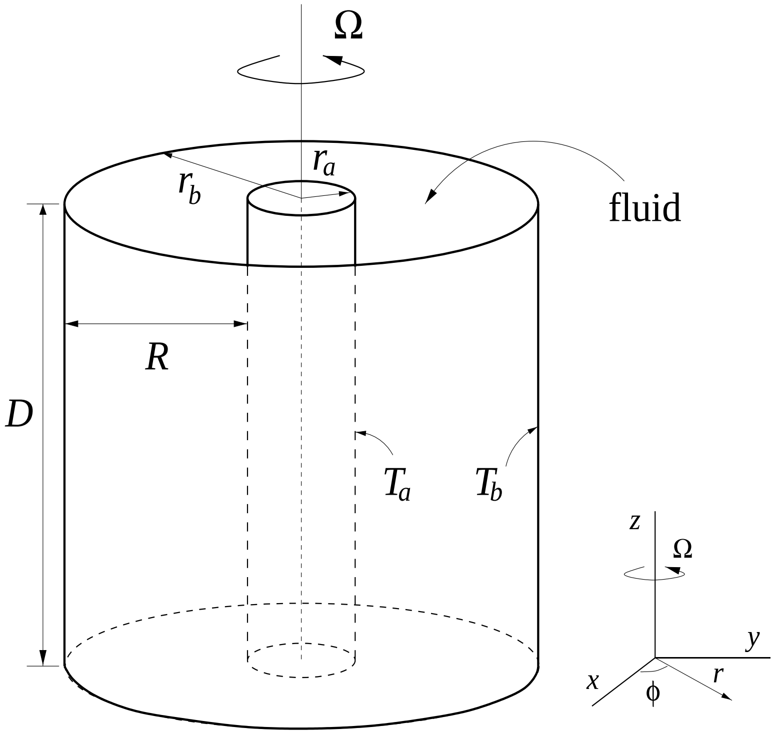

FIG. 2.1. *The differentially heated rotating annulus experiment, where the annulus is rotated at rate $\Omega$ and the inner wall is held at the fixed temperature $T_a$ and the outer wall at temperature $T_b$, creating a differential heating $\Delta T = T_b - T_a$. $r_a$ and $r_b$ are the radii of the inner and outer cylinders, $R = r_b - r_a$, and $D$ is the height of the annulus.*

Of particular interest to us, is the transition from the axisymmetric to wave regime and the hysteresis of the waves which is observed in the steady wave regime. The hysteresis occurs between waves whose wave numbers differ by the integer one. By quantifying the double Hopf bifurcations that occur along the transition, we give evidence of the mechanism by which the hysteresis occurs.

**3. Model Equations.** The dynamical equations of the fluid are taken to be the Navier-Stokes equations in the Boussinesq approximation. In particular, we consider the variations of all fluid properties to be negligible, and the equation of state of the fluid is assumed to be

$$\rho = \rho_0[1 - \alpha\,(T - T_0)] \tag{3.1}$$

where $\rho$ is the density of the fluid, $T$ is the temperature, $\alpha$ is the (constant) coefficient of thermal expansion, $\rho_0$ is the density at the reference temperature $T_0$, and $\alpha\,(T - T_0)$ is assumed to be small. A significant simplification due to the Boussinesq approximation is that the fluid can be considered incompressible. For the temperature evolution, we take the heat equation, with an advection term that couples the fluid velocity to the temperature. The boundaries are the inner wall of the cylindrical annulus with radius $r_a$, the outer wall with radius $r_b$, as well as a rigid flat bottom and top. At the boundaries, the no-slip condition is imposed on the fluid, and the temperature is $T_a$ and $T_b$ at the inner and outer walls, respectively, while the bottom

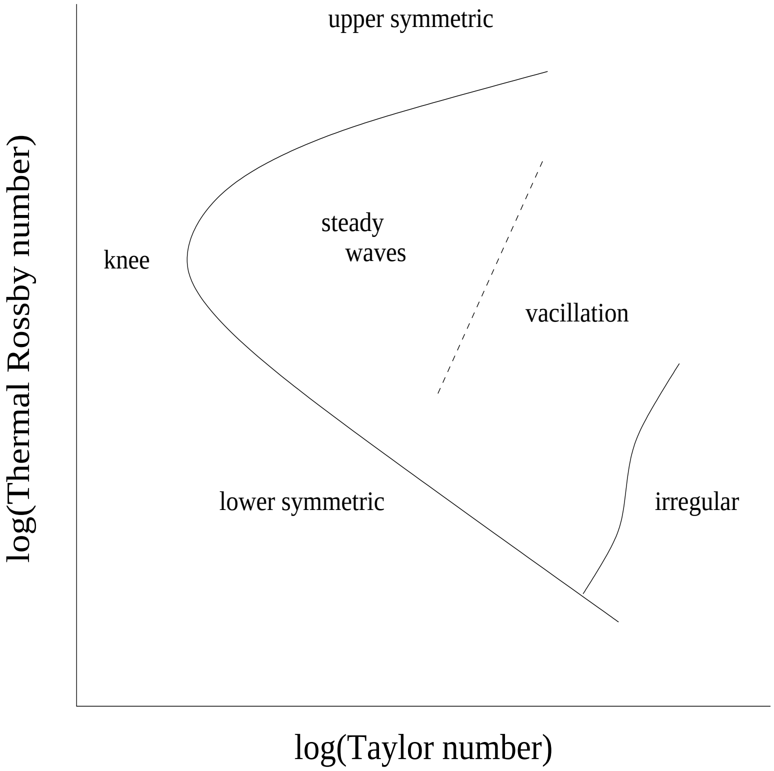

FIG. 2.2. *A schematic diagram depicting general experimental results. See* e.g. *[13]. To the left of all the curves is the axisymmetric regime which is separated into three (dynamically similar) regions: lower symmetric, knee, and upper symmetric. To the right of the curve is the non-axisymmetric regime which is separated into three dynamically distinct regimes: steady waves, vacillation and irregular flow.*

and top are thermally insulating. The equations are written in circular cylindrical coordinates in a frame of reference co-rotating with the annulus at rate $\Omega$. The radial, azimuthal and vertical (or axial) coordinates are denoted $r$, $\varphi$ and $z$, respectively, with unit vectors $\mathbf{e}_r$, $\mathbf{e}_\varphi$ and $\mathbf{e}_z$. See Figure 2.1.

We make a change of variables

$$r = Rr', \quad z = Dz', \tag{3.2}$$

where $R = r_b - r_a$ is the gap width and $D$ is the height of the annulus, write the fluid temperature as

$$T = T'(r', \varphi, z', t) + \Delta T \left(r' - \frac{r_a}{R}\right) + T_a, \tag{3.3}$$

where $\Delta T = T_b - T_a$ is the imposed temperature difference, and write the fluid pressure as

$$p = p'(r', \varphi, z', t) + \rho_0 g D(1 - z') + \rho_0 \Omega^2 R^2 (r')^2/2. \tag{3.4}$$

Then we drop the primes, to obtain equations describing the evolution of the fluid velocity $\mathbf{u} = u(r,\varphi,z,t)\mathbf{e}_r + v(r,\varphi,z,t)\mathbf{e}_\varphi + w(r,\varphi,z,t)\mathbf{e}_z$, pressure deviation $p =$

$p(r,\varphi,z,t)$ and temperature deviation $T=T(r,\varphi,z,t)$:

$$\begin{aligned}
&(3.5)\quad \frac{\partial \mathbf{u}}{\partial t} = \nu_s\nabla_s^2\mathbf{u} - \frac{1}{R\rho_0}\nabla_s p - 2\Omega\mathbf{e}_z\times\mathbf{u}\\
&\qquad\qquad + \left(g\mathbf{e}_z - \Omega^2 Rr\mathbf{e}_r\right)\alpha\left[T+\Delta T\left(r-\frac{r_a}{R}\right)+T_a-T_0\right] - \frac{1}{R}\left(\mathbf{u}\cdot\nabla_s\right)\mathbf{u},\\
&(3.6)\quad \frac{\partial T}{\partial t} = \kappa_s\nabla_s^2 T + \kappa_s\frac{\Delta T}{r} - \frac{\Delta T}{R}u - \frac{1}{R}\left(\mathbf{u}\cdot\nabla_s\right)T,\\
&(3.7)\quad \nabla_s\cdot\mathbf{u} = \frac{\partial u}{\partial r}+\frac{u}{r}+\frac{\partial v}{\partial\varphi}+\frac{1}{\delta}\frac{\partial w}{\partial z}=0,
\end{aligned}$$

where $\delta = D/R$, $\nu_s = \nu/R^2$, $\nu$ is the kinematic viscosity, $\kappa_s=\kappa/R^2$, $\kappa$ is the coefficient of thermal diffusivity, $g$ is the gravitational acceleration,

$$\nabla_s^2 = \frac{\partial^2}{\partial r^2}+\frac{1}{r}\frac{\partial}{\partial r}+\frac{1}{r^2}\frac{\partial^2}{\partial\varphi^2}+\frac{1}{\delta^2}\frac{\partial^2}{\partial z^2},$$

$$\nabla_s = \mathbf{e}_r\frac{\partial}{\partial r}+\mathbf{e}_\varphi\frac{1}{r}\frac{\partial}{\partial\varphi}+\mathbf{e}_z\frac{1}{\delta}\frac{\partial}{\partial z},$$

$$\begin{aligned}
\left(\mathbf{u}_1\cdot\nabla_s\right)\mathbf{u}_2 = &\left(u_1\frac{\partial u_2}{\partial r}+\frac{v_1}{r}\frac{\partial u_2}{\partial\varphi}+\frac{1}{\delta}w_1\frac{\partial u_2}{\partial z}-\frac{v_1v_2}{r}\right)\mathbf{e}_r\\
&+\left(u_1\frac{\partial v_2}{\partial r}+\frac{v_1}{r}\frac{\partial v_2}{\partial\varphi}+\frac{1}{\delta}w_1\frac{\partial v_2}{\partial z}+\frac{u_1v_2}{r}\right)\mathbf{e}_\varphi\\
&+\left(u_1\frac{\partial w_2}{\partial r}+\frac{v_1}{r}\frac{\partial w_2}{\partial\varphi}+\frac{1}{\delta}w_1\frac{\partial w_2}{\partial z}\right)\mathbf{e}_z,
\end{aligned}$$

for velocity fields $\mathbf{u}_j = u_j(r,\varphi,z,t)\mathbf{e}_r + v_j(r,\varphi,z,t)\mathbf{e}_\varphi + w_j(r,\varphi,z,t)\mathbf{e}_z$, $j=1,2$, and

$$\left(\mathbf{u}\cdot\nabla_s\right)T = u\frac{\partial T}{\partial r}+\frac{v}{r}\frac{\partial T}{\partial\varphi}+\frac{1}{\delta}w\frac{\partial T}{\partial z}.$$

The domain is $r_a/R<r<r_b/R$, $0\le\varphi<2\pi$, $0<z<1$, and the boundary conditions are

$$\begin{aligned}
&(3.8)\qquad \mathbf{u}=0 \quad\text{on}\quad r=\frac{r_a}{R},\ \frac{r_b}{R}\quad\text{and}\quad z=0,1,\\
&\qquad\qquad T=0 \quad\text{on}\quad r=\frac{r_a}{R},\ \frac{r_b}{R},\\
&\qquad\qquad \frac{\partial T}{\partial z}=0 \quad\text{on}\quad z=0,1,
\end{aligned}$$

with $2\pi$-periodicity in $\varphi$ for $\mathbf{u}$, $T$ and $p$.

The solutions will not depend explicitly on the value of the reference temperature $T_0$. However, there is implicit dependence because the values of $\nu$, $\kappa$ and $\rho_0$ are chosen to be those of the fluid at $T_0$. It is assumed that the difference between the temperature of the fluid and $T_0$ is everywhere small enough so that $\nu$ and $\kappa$ can be considered as constants.

**4. Analytical Methods.** We choose as the parameters of interest the rotation rate $\Omega$ and the temperature difference $\Delta T$ between the inner and outer annulus walls. These are the physical quantities (external variables) that are easily varied in an experiment. The other parameters describe the geometry of the annulus or properties of the fluid. Another choice is to use the dimensionless parameters, the Taylor number $\mathcal{T}$ and the thermal Rossby number $\mathcal{R}$ (see Section 2), which have a one-to-one correspondence with $\Omega$ and $\Delta T$. Our results are quoted in terms of these dimensionless parameters because experimental results are usually presented on a log-log plot of $\mathcal{T}$ versus $\mathcal{R}$. However, the analysis was carried out using the parameters $\Omega$ and $\Delta T$, because non-dimensionalization did not significantly simplify the equations (see [18]). The choice of parameters will not change the procedure or the results.

A summary of the main steps of the analysis is as follows:

1. Plot the neutral stability curves, by
   (a) calculating the steady axisymmetric solution at a particular location in parameter space,
   (b) solving the eigenvalue problem for this solution to find its linear stability,
   (c) repeating steps (a) and (b) at various locations in parameter space to find the parameter values where the solution is neutrally stable.
2. Localize the point in parameter space where the double Hopf bifurcation occurs (find the intersections of the neutral stability curves; see below).
3. Calculate the eigenvalues and eigenfunctions at the bifurcation point.
4. Compute the appropriate normal form coefficients, which involves
   (a) calculating the adjoint eigenfunctions,
   (b) calculating the center manifold coefficients.

An analytical form for the steady axisymmetric solution is not known, and, therefore, numerical approximations must be made. This is also the case for the eigenvalues and eigenfunctions. In the analysis, this is dealt with by leaving the the unknown functions unresolved when deriving the formulae for the normal form coefficients. That is, we write the normal form coefficients in terms of the unresolved functions. Then, for the numerical approximation of the normal form coefficients, the values of the unknown functions are only needed at specific locations (the grid points), and numerical approximations are used. We postpone discussion of the numerical methods until the next section, and for the remainder of this section, we discuss the analytical methods. In particular, we discuss the equations necessary for the computation of the axisymmetric solution and the eigenfunctions, and we discuss briefly how center manifold reduction is used to derive the formulae for the normal form coefficients of interest. For a more detailed explanation of the center manifold reduction and normal form equations in the context of this model, see [18] and for a general context see *e.g.* [11].

**4.1. The steady axisymmetric solution.** The analysis begins with the computation of a steady axisymmetric solution. That is, we look for a solution of equations (3.5)–(3.7), with the boundary conditions (3.8), in the form

$$\mathbf{u} = \mathbf{u}^{(0)}(r,z) = u^{(0)}(r,z)\mathbf{e}_r + v^{(0)}(r,z)\mathbf{e}_\varphi + w^{(0)}(r,z)\mathbf{e}_z,$$

$$p = p^{(0)}(r,z), \quad T = T^{(0)}(r,z),$$

independent of $\varphi$ and $t$. The solution also depends on the parameters, but we do not indicate this dependence explicitly. We assume that such a solution exists, is unique and regular, and depends smoothly on the parameters, at least for the parameter values of interest. We have not attempted to prove this, but believe that, using standard techniques, it would be a feasible if lengthy digression to do so (see, for example [3]).

A stream function $\xi^{(0)}$ is introduced, so that the incompressibility condition (3.7) is automatically satisfied. The pressure terms can then be eliminated, and we obtain three equations in the three unknown functions $\xi^{(0)}$, $v^{(0)}$ and $T^{(0)}$. The resulting equations, computed using the Maple symbolic computation package, are sufficiently complicated that no insight is gained by explicitly writing them here. For more details, see [18]. In Section 5, we describe how $\xi^{(0)}$, $v^{(0)}$ and $T^{(0)}$ are computed numerically.

**4.2. The perturbation equations.** Next, the perturbation equations are required. It is on this system that the center manifold reduction is performed. We write

$$\mathbf{u} = \mathbf{u}^{(0)} + \hat{\mathbf{u}}, \quad p = p^{(0)} + \hat{p}, \quad T = T^{(0)} + \hat{T}, \tag{4.1}$$

where $(\mathbf{u}^{(0)}, p^{(0)}, T^{(0)})$ is the steady axisymmetric solution, substitute (4.1) into equations (3.5)–(3.7), and drop the hats, to obtain the perturbation equations

$$\begin{aligned}\frac{\partial \mathbf{u}}{\partial t} &= \nu_s \nabla_s^2 \mathbf{u} - \frac{1}{R\rho_0}\nabla_s p - 2\Omega \mathbf{e}_z \times \mathbf{u} + \left(g\mathbf{e}_z - \Omega^2 Rr\mathbf{e}_r\right)\alpha T \\ &\quad - \frac{1}{R}\left(\mathbf{u}^{(0)}\cdot\nabla_s\right)\mathbf{u} - \frac{1}{R}\left(\mathbf{u}\cdot\nabla_s\right)\mathbf{u}^{(0)} - \frac{1}{R}\left(\mathbf{u}\cdot\nabla_s\right)\mathbf{u},\end{aligned} \tag{4.2}$$

$$\frac{\partial T}{\partial t} = \kappa_s \nabla_s^2 T - \frac{\Delta T}{R} u - \frac{1}{R}\left(\mathbf{u}^{(0)}\cdot\nabla_s\right)T - \frac{1}{R}\left(\mathbf{u}\cdot\nabla_s\right)T^{(0)} - \frac{1}{R}\left(\mathbf{u}\cdot\nabla_s\right)T, \tag{4.3}$$

$$\nabla_s \cdot \mathbf{u} = 0, \tag{4.4}$$

with the boundary conditions (3.8). The trivial solution $\mathbf{u} = \mathbf{0}$, $p = 0$, $T = 0$ now satisfies these equations, and corresponds to the steady axisymmetric solution of equations (3.5)–(3.7).

The perturbation equations (4.2)–(4.4) can be put into a suitable abstract form for which some important theoretical properties have been established. Following Henry [12, pp. 79–81], we can define a space $\mathcal{X}$ of vector functions $U = [\mathbf{u}, T]$ so that the incompressibility condition (4.4) and boundary conditions (3.8) are satisfied as part of the definition of the space. Then there is an abstract projection operator onto the space $\mathcal{X}$ that eliminates the pressure terms, and the system (4.2)–(4.4) together with boundary conditions (3.8) can be written as an abstract evolution equation in the space $\mathcal{X}$,

$$\dot{U} = \mathbf{L}\,U + \mathbf{N}(U), \tag{4.5}$$

where $\mathbf{L}\,U$ is the linear part of the equation (observe that $\mathbf{L}$ depends on the parameters, through the steady axisymmetric solution), and $\mathbf{N}(U)$ is the nonlinear part (it has the form $\mathbf{N}(U) = \mathbf{M}(U, U)$, where $\mathbf{M}$ is bilinear). If we assume that the steady axisymmetric solution of (3.5)–(3.8) exists, is unique, is regular, and depends smoothly on the parameters, then at least locally near $U = 0$ the initial-value problem for (4.5) in $\mathcal{X}$ has a unique solution $U(t)$, $t \geq 0$, that depends smoothly on initial conditions and parameters [12, Chapter 3]. Moreover, the principle of linearized stability holds, and the stability of the trivial solution $U = 0$ of (4.5) can be determined from the spectrum of the linearization $\mathbf{L}$ [12, Chapter 5].

**4.3. The eigenvalue problem.** The linearized stability of the steady axisymmetric solution is determined by the spectrum of the linearization of (4.2)–(4.4) about the trivial solution. Since $\mathbf{L}$ is the sum of a self-adjoint operator and a bounded linear operator, it is sectorial. The spatial domain is bounded, so the spectrum consists entirely of isolated eigenvalues of finite multiplicity. The eigenvalue problem is formally obtained by assuming that the unknown functions may be written as $\mathbf{u} = \mathbf{u}(r, \varphi, z, t) = e^{\lambda t}\tilde{\mathbf{u}}_m(r, z)e^{im\varphi}$, with $m$ an integer, and likewise for $T$ and $p$, and then linearizing (4.2)–(4.4). A linear eigenvalue problem, for the eigenvalues $\lambda$ and the eigenfunctions $\left[\tilde{\mathbf{u}}_m(r, z), \tilde{T}_m(r, z)\right] e^{im\varphi}$, is obtained for each azimuthal wave number $m$. By the principle of linearized stability, if all eigenvalues $\lambda$ have negative real parts, then the steady axisymmetric solution is asymptotically stable, while if any eigenvalue $\lambda$ has a positive real part, then the steady axisymmetric solution is unstable. We are especially interested in locating critical parameter values where a finite number of eigenvalues have zero real parts, and the rest have negative real parts. The solution is then neutrally stable, and we expect bifurcation of solutions of the nonlinear equations as parameters are varied near the critical values. The azimuthal wave numbers $m$ of the eigenfunctions corresponding to the eigenvalues that have zero real part at the critical parameter values are defined as the critical wave numbers.

If $m \neq 0$, it is possible to eliminate the pressure and azimuthal velocity terms. The resulting three equations in the three remaining unknowns $\tilde{u}_m(r, z)$, $\tilde{w}_m(r, z)$ and $\tilde{T}_m(r, z)$ may be written in the form of a generalized linear eigenvalue problem

$$\lambda \mathbf{A}_m \tilde{U}_m = \mathbf{L}_m \tilde{U}_m, \tag{4.6}$$

where

$$\tilde{U}_m = \begin{pmatrix} \tilde{u}_m \\ \tilde{w}_m \\ \tilde{T}_m \end{pmatrix},$$

and $\mathbf{A}_m$ and $\mathbf{L}_m$ are $3 \times 3$ matrices of linear operators. If $m = 0$, a stream function method can be used in exactly the same manner as in the calculation of the axisymmetric solution. Again the equations were calculated using Maple and are too lengthy to write here.

Finally, the adjoint eigenvalue problem is necessary to calculate the adjoint eigenfunctions. The adjoint operators are calculated using the inner product, which for two vector functions $U_1 = [\mathbf{u}_1, T_1]$ and $U_2 = [\mathbf{u}_2, T_2]$ is taken to be

$$\langle U_1, U_2 \rangle = \int_0^1 \int_0^{2\pi} \int_{\frac{r_a}{R}}^{\frac{r_b}{R}} \left(\mathbf{u}_1 \cdot \overline{\mathbf{u}}_2 + T_1 \overline{T}_2\right) r \; dr \; d\varphi \; dz, \tag{4.7}$$

where the overbar denotes complex conjugation. The adjoint eigenfunctions have the form $\left[\tilde{\mathbf{u}}^*_m(r, z), \tilde{T}^*_m(r, z)\right] e^{im\varphi}$.

**4.4. Normal form coefficients.** The numerical results, presented in Section 6, predict that there are critical parameter values where the linear eigenvalue problem has two complex conjugate pairs of eigenvalues with zero real parts, while the other eigenvalues have negative real parts. Therefore, suppose that the critical parameter values occur at $\Omega = \Omega_0$ and $\Delta T = \Delta T_0$, so that for $\Omega$ near $\Omega_0$ and $\Delta T$ near $\Delta T_0$, the eigenvalue problem has eigenvalues

$$\lambda_1 = \mu_1 + i\omega_1, \quad \overline{\lambda}_1, \quad \lambda_2 = \mu_2 + i\omega_2, \quad \overline{\lambda}_2, \tag{4.8}$$

and when $\Omega = \Omega_0$ and $\Delta T = \Delta T_0$, we have $\mu_1 = \mu_2 = 0$. Also, assume that all the other eigenvalues have negative real parts, with the real parts uniformly bounded below zero.

The eigenfunctions corresponding to the above eigenvalues are

$$\Phi_1, \quad \overline{\Phi}_1, \quad \Phi_2, \quad \overline{\Phi}_2,$$

where they have the form

$$\Phi_j = \left[\tilde{\mathbf{u}}_{m_j}(r,z), \tilde{T}_{m_j}(r,z)\right] e^{im_j\varphi},$$

with $m_j$ ($j = 1, 2,\ m_1 \neq m_2$) being the azimuthal wave number corresponding to $\Phi_j$. The center eigenspace $E^c$ is the span of the eigenfunctions corresponding to the eigenvalues with zero real parts when $\Omega = \Omega_0$ and $\Delta T = \Delta T_0$,

$$E^c = \operatorname{span}\{\Phi_1, \overline{\Phi}_1, \Phi_2, \overline{\Phi}_2\}.$$

The stable eigenspace $E^s$ is the span of all the other eigenfunctions that correspond to eigenvalues with negative real parts. The adjoint eigenfunctions corresponding to the $\Phi_j$ are denoted by $\Phi_j^*$, where the $\Phi_j^*$ are found from the adjoint eigenvalue problem. The eigenfunctions and their adjoints are normalized so that their inner products satisfy

$$\langle \Phi_j, \Phi_j^* \rangle = 1, \tag{4.9}$$

for $j = 1, 2$. Due to a rescaling (see below), the results do not depend on the way in which the second normalization constant is determined.

The projection of $U$ onto the center eigenspace $E^c$ is given by

$$PU = \langle U, \Phi_1^* \rangle \Phi_1 + \langle U, \overline{\Phi}_1^* \rangle \overline{\Phi}_1 + \langle U, \Phi_2^* \rangle \Phi_2 + \langle U, \overline{\Phi}_2^* \rangle \overline{\Phi}_2. \tag{4.10}$$

Using this projection, we may then decompose $U$:

$$U = z_1\Phi_1 + \overline{z}_1\overline{\Phi}_1 + z_2\Phi_2 + \overline{z}_2\overline{\Phi}_2 + \Psi, \tag{4.11}$$

where $PU = z_1\Phi_1 + \overline{z}_1\overline{\Phi}_1 + z_2\Phi_2 + \overline{z}_2\overline{\Phi}_2 \in E^c$ and $(I - P)U = \Psi \in E^s$, and $I$ is the identity operator. This implies that the complex amplitudes $z_1$ and $z_2$ are given by the inner products $z_1 = z_1(t) = \langle U, \Phi_1^* \rangle$ and $z_2 = z_2(t) = \langle U, \Phi_2^* \rangle$.

Taking the projection of equation (4.5), we get

$$\begin{aligned} \dot{z}_1 &= \lambda_1 z_1 + \langle \mathbf{N}(U), \Phi_1^* \rangle, \\ \dot{z}_2 &= \lambda_2 z_2 + \langle \mathbf{N}(U), \Phi_2^* \rangle, \end{aligned} \tag{4.12}$$

where $U$ is given by (4.11). The complex conjugate equations contain redundant information, and so are omitted. For (4.12), we use center manifold theory to write $U$ solely in terms of the center eigenspace variables $z_1$ and $z_2$, and in so doing we decouple the system.

Given that the assumptions stated above for (4.5) and the eigenvalues for the linearization are valid, then, for $(\Omega, \Delta T)$ in a neighborhood of $(\Omega_0, \Delta T_0)$, the center manifold theorem [12, p. 168] implies that there exists a differentiable center manifold for equation (4.5) :

$$W_{loc}^c = \left\{U = z_1\Phi_1 + \overline{z}_1\overline{\Phi}_1 + z_2\Phi_2 + \overline{z}_2\overline{\Phi}_2 + H(z_1\Phi_1, \overline{z}_1\overline{\Phi}_1, z_2\Phi_2, \overline{z}_2\overline{\Phi}_2)\right\}, \tag{4.13}$$

where $H : E^c \to E^s$ is defined for $\|z_1\Phi_1 + \overline{z}_1\overline{\Phi}_1 + z_2\Phi_2 + \overline{z}_2\overline{\Phi}_2\|$ small and $\|\cdot\|$ is the norm that corresponds to the inner product (4.7). The local center manifold $W^c_{loc}$ is locally invariant, is tangent to the center eigenspace $E^c$ at $U = 0$ when $\Omega = \Omega_0$ and $\Delta T = \Delta T_0$, and is locally exponentially attracting.

Therefore, on the center manifold, we can write

$$\Psi = H(z_1, \overline{z}_1, z_2, \overline{z}_2) = O(|z_1, \overline{z}_1, z_2, \overline{z}_2|^2) \tag{4.14}$$

and then expand the center manifold function $H$ in a Taylor series as

$$\begin{aligned} H(z_1, \overline{z}_1, z_2, \overline{z}_2) = {} & H_{2000}z_1^2 + H_{1100}z_1\overline{z}_1 + H_{0020}z_2^2 + H_{0011}z_2\overline{z}_2 \\ & + H_{1010}z_1z_2 + H_{1001}z_1\overline{z}_2 + c.c. + O(3), \end{aligned} \tag{4.15}$$

where $H_{ijkl}$ are the Taylor series coefficients of $H$, $O(n) = O(|z_1, \overline{z}_1, z_2, \overline{z}_2|^n)$ and *c.c.* denotes the complex conjugates of the previous terms that are written explicitly. We also write

$$\begin{aligned} N(z_1, \overline{z}_1, z_2, \overline{z}_2) = {} & N_{2000}z_1^2 + N_{1100}z_1\overline{z}_1 + N_{0020}z_2^2 + N_{0011}z_2\overline{z}_2 \\ & + N_{1010}z_1z_2 + N_{1001}z_1\overline{z}_2 + c.c. + O(3), \end{aligned} \tag{4.16}$$

where $N(z_1, \overline{z}_1, z_2, \overline{z}_2)$ is the nonlinear term of (4.5) written in terms of $z_1, \overline{z}_1, z_2$ and $\overline{z}_2$, using the decomposition of $U$ given in equation (4.11), and with $\Psi$ written using (4.14) and (4.15). With the nonlinear part written as (4.16), the system is decoupled and (4.12) reduces to a four-dimensional ordinary differential equation that describes the dynamics on the center manifold. Because the center manifold is locally exponentially attracting, the behaviour of the original partial differential equations, close to the bifurcation point, can be deduced from the reduced system.

The normal form for the non-resonant case is

$$\begin{aligned} \dot{z}_1 &= \lambda_1 z_1 + G_{11}z_1^2\overline{z}_1 + G_{12}z_1z_2\overline{z}_2 + O(4), \\ \dot{z}_2 &= \lambda_2 z_2 + G_{21}z_1\overline{z}_1z_2 + G_{22}z_2^2\overline{z}_2 + O(4), \end{aligned} \tag{4.17}$$

where $\lambda_j{=}\lambda_j(\Omega, \Delta T)$, and the normal form coefficients $G_{kl}$ are given by

$$\begin{aligned} G_{11} &= \langle N_{2100}, \Phi_1^*\rangle, \\ G_{12} &= \langle N_{1011}, \Phi_1^*\rangle, \\ G_{21} &= \langle N_{1110}, \Phi_2^*\rangle, \\ G_{22} &= \langle N_{0021}, \Phi_2^*\rangle. \end{aligned} \tag{4.18}$$

The normal form (4.17) is obtained from (4.12) by using a series of near-identity coordinate transformations (see, *e.g.*, [26]). This normal form requires the non-resonance condition that the imaginary parts of the eigenvalues, $\omega_1$ and $\omega_2$, satisfy $n_1\omega_1 {+} n_2\omega_2 \neq 0$ for all integers $n_1$ and $n_2$ with $|n_1| {+} |n_2| \leq 4$, at the critical parameter values $\Omega = \Omega_0$ and $\Delta T = \Delta T_0$.

In general, the formulae (4.18) for the normal form coefficients also depend on the coefficients of the terms that are quadratic in $z_1$ and $z_2$ (*e.g.* $N_{2000}$). However, in our case these terms vanish in the projection (4.12), because, due to their $\varphi$-dependence, they are orthogonal to the adjoint eigenfunctions. In the same manner it can be shown that to find the normal form coefficient $G_{11} = \langle N_{2100}, \Phi_1^*\rangle$, only $\tilde{N}^{(m_1)}_{2100}$ is needed, where $\tilde{N}^{(m_1)}_{ijkl}$ is defined as the coefficient of $e^{im_1\varphi}$ in the expansion $N_{ijkl}(r, \varphi, z) =$

$\sum_m \tilde{N}_{ijkl}^{(m)}(r,z)\, e^{im\varphi}$. That is, all terms with a factor $e^{im\varphi}$, $m \neq m_1$, vanish in the inner product because they are orthogonal to $\Phi_1^*$. Furthermore, due to the form of the nonlinear part, only the eigenfunctions $\Phi_1$, $\overline{\Phi}_1$, and the particular coefficients of the center manifold function, $\tilde{H}_{1100}^{(0)}$ and $\tilde{H}_{2000}^{(2m_1)}$, appear in the formula for $\tilde{N}_{2100}^{(m_1)}$, where the $\tilde{H}_{ijkl}^{(m)}$ are defined in a similar manner as the $\tilde{N}_{ijkl}^{(m)}$, *i.e.* $H_{ijkl}(r,\varphi,z) = \sum_m \tilde{H}_{ijkl}^{(m)}(r,z)\, e^{im\varphi}$.

Thus, in addition to the eigenfunctions, the normal form coefficient

- $G_{11}$ can be written as a function of only the coefficients $\tilde{H}_{1100}^{(0)}$ and $\tilde{H}_{2000}^{(2m_1)}$.

Similarly, in addition to the eigenfunctions, the normal form coefficients

- $G_{12}$ can be written as a function of only the coefficients, $\tilde{H}_{0011}^{(0)}$, $\tilde{H}_{1001}^{(m_1-m_2)}$ and $\tilde{H}_{1010}^{(m_1+m_2)}$,
- $G_{21}$ can be written as a function of only the coefficients $\tilde{H}_{1100}^{(0)}$, $\tilde{H}_{0110}^{(m_2-m_1)}$ and $\tilde{H}_{1010}^{(m_1+m_2)}$,
- $G_{22}$ can be written as a function of only the coefficients $\tilde{H}_{0011}^{(0)}$ and $\tilde{H}_{0020}^{(2m_2)}$.

The equations satisfied by the $H_{ijkl}(r,\varphi,z)$ are derived using the local invariance of the center manifold [11]. From these equations, it follows that the relevant $\tilde{H}_{ijkl}^{(m)}(r,z)$ satisfy:

$$\begin{aligned}
\left[2\lambda_1 \mathbf{I} - \tilde{\mathbf{L}}^{(2m_1)}\right] \tilde{H}_{2000}^{(2m_1)} &= \tilde{N}_{2000}^{(2m_1)}, \\
\tilde{\mathbf{L}}^{(0)} \tilde{H}_{1100}^{(0)} &= -\tilde{N}_{1100}^{(0)}, \\
\left[2\lambda_2 \mathbf{I} - \tilde{\mathbf{L}}^{(2m_2)}\right] \tilde{H}_{0020}^{(2m_2)} &= \tilde{N}_{0020}^{(2m_2)}, \\
\tilde{\mathbf{L}}^{(0)} \tilde{H}_{0011}^{(0)} &= -\tilde{N}_{0011}^{(0)}, \\
\left[(\lambda_1 + \lambda_2)\mathbf{I} - \tilde{\mathbf{L}}^{(m_1+m_2)}\right] \tilde{H}_{1010}^{(m_1+m_2)} &= \tilde{N}_{1010}^{(m_1+m_2)}, \\
\left[(\lambda_1 + \overline{\lambda}_2)\mathbf{I} - \tilde{\mathbf{L}}^{(m_1-m_2)}\right] \tilde{H}_{1001}^{(m_1-m_2)} &= \tilde{N}_{1001}^{(m_1-m_2)},
\end{aligned} \tag{4.19}$$

where the $\tilde{\mathbf{L}}^{(m)}$ are defined by $\mathbf{L}\left[\tilde{U}(r,z)e^{im\varphi}\right] = e^{im\varphi}\left[\tilde{\mathbf{L}}^{(m)}\tilde{U}(r,z)\right]$ and $\mathbf{I}$ is the identity operator. For $m \neq 0$, the same solution method that is used for the eigenvalue problem can be used here (*i.e.* elimination of the pressure term and one velocity component). For $m = 0$, the stream function method (as for the axisymmetric solution) can be used.

We write $z_1 = \rho_1 e^{i\theta_1}/\sqrt{|G_{11}^r|}$ and $z_2 = \rho_2 e^{i\theta_2}/\sqrt{|G_{22}^r|}$, where $G_{ij}^r$ is the real part of the normal form coefficients $G_{ij}$, and substitute these expressions into (4.17). In these scaled polar coordinates, the truncated normal form equations are

$$\begin{aligned}
\dot{\rho}_1 &= \rho_1\left(\mu_1 + a\rho_1^2 + b\rho_2^2\right), \\
\dot{\rho}_2 &= \rho_2\left(\mu_2 + c\rho_1^2 + d\rho_2^2\right), \\
\dot{\theta}_1 &= \omega_1, \\
\dot{\theta}_2 &= \omega_2,
\end{aligned} \tag{4.20}$$

where

$$a = \frac{G_{11}^r}{|G_{11}^r|} = \pm 1, \tag{4.21}$$

$$\begin{aligned} b &= \frac{G^r_{12}}{|G^r_{22}|}, \\ c &= \frac{G^r_{21}}{|G^r_{11}|}, \\ d &= \frac{G^r_{22}}{|G^r_{22}|} = \pm 1, \end{aligned}$$

and $\lambda_j = \mu_j + i\omega_j$. The $O(|\rho_1, \rho_2|^4)$ terms are ignored in the $\dot{\rho}_j$ equations, and the $O(|\rho_1, \rho_2|^2)$ terms are ignored in the $\dot{\theta}_j$ equations. Ignoring these terms does not affect the local dynamics, except for fine details of the dynamics on invariant tori.

In summary, given $m_1$ and $m_2$, the coefficients of the scaled normal form equations $a, b, c, d$ can be written in terms of the following functions, which are all only functions of two spatial variables $r$ and $z$:

- the eigenfunctions and adjoint eigenfunctions

$$\tilde{\Phi}_{m_1}, \quad \tilde{\Phi}^*_{m_1}, \quad \tilde{\Phi}_{m_2}, \quad \tilde{\Phi}^*_{m_2},$$

  where $\Phi_j(r, \varphi, z) = \tilde{\Phi}_{m_j}(r, z) e^{i m_j \varphi}$, $j = 1, 2$.
- certain Taylor series coefficients of the center manifold function

$$\tilde{H}^{(0)}_{1100}, \quad \tilde{H}^{(2m_1)}_{2000}, \quad \tilde{H}^{(m_1 - m_2)}_{1001}, \quad \tilde{H}^{(m_1 + m_2)}_{1010}, \quad \tilde{H}^{(0)}_{0011} \text{ and } \tilde{H}^{(2m_2)}_{0020},$$

where $H_{ijkl}(r, \varphi, z) = \sum_m \tilde{H}^{(m)}_{ijkl}(r, z) e^{i m \varphi}$. The eigenfunctions are found from the eigenvalue problem (4.6), and the coefficients of the center manifold function are found from (4.19).

## 5. Numerical Methods.

In order to find values of the normal form coefficients, the axisymmetric solution, the eigenfunctions and the Taylor series coefficients of the center manifold function must be known. Because analytic solutions of these are not known, they are approximated numerically. Upon discretization, the axisymmetric solution is approximated from a system of nonlinear algebraic equations, while the partial differential eigenvalue problems become matrix eigenvalue problems and the partial differential boundary value problems for finding the coefficients of the center manifold function become systems of linear equations. In all cases, the discretization leads to large sparse systems, and so, we seek appropriate solution techniques.

In this section, we discuss some of the details of the numerical approximations, including the discretization and solution techniques. Also included is a brief discussion of convergence for the approximation.

### 5.1. The mesh: non-uniform spacing.

We employ centered finite differencing to discretize the spatial derivatives. The values of the unknown functions, in the interior of the domain, are approximated at $N \times N$ grid points, labeled by $(r, z) = (r_k, z_l)$, with $1 \le k \le N$ and $1 \le l \le N$, where $N$, $k$, $l$ are positive integers. We define $r_0 = r_a/R$, $r_{N+1} = r_b/R$, $z_0 = 0$ and $z_{N+1} = 1$. This leads to a discretized solution vector of size $3N^2 + 2N$ (because $T(r_k, z_0)$ and $T(r_k, z_{N+1})$ are also unknown for $1 \le k \le N$).

With the no-slip boundary conditions and the small parameter $\nu$ multiplying a second derivative term, boundary layers form in the fluid flow. For this reason, a scaling method is used to choose the locations of the grid points. This consists of making a change of coordinates and calculating the solutions on a uniform grid in the new coordinates. The transformation is chosen such that its inverse takes a uniform grid to a grid with many points near the boundary. The transformation that takes the new coordinates $(x, y)$ to the original coordinates $(r, z)$ is given by

$$r = \frac{\tan^{-1}(\eta x)}{2\tan^{-1}\left(\frac{\eta}{2}\right)} + \frac{1}{2} + \frac{r_a}{R}, \qquad z = \frac{\tan^{-1}(\eta y)}{2\tan^{-1}\left(\frac{\eta}{2}\right)} + \frac{1}{2}, \tag{5.1}$$

where $\eta$ is a scaling factor that determines the magnitude of compression near the boundary. See Figure 5.1. The domain $r_a \leq r \leq r_b/R$, $0 \leq z \leq 1$ is mapped to $-1/2 \leq x \leq 1/2$, $-1/2 \leq y \leq 1/2$, and the solutions are approximated on a uniform grid in the $(x, y)$ coordinates.

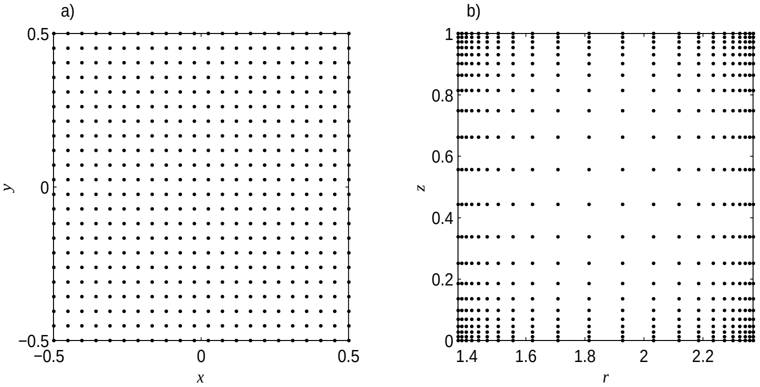

FIG. 5.1. *The transformation of the grid points. (a) A uniform grid (equally spaced grid points) of $N = 20$ (b) the grid obtained by applying the change of coordinates (5.1) with $\eta = 6$.*

The boundary layers observed in the eigenfunctions are not as severe as those in the axisymmetric solutions. In fact, significant errors are introduced in the eigenvalues and eigenfunctions if the points in the interior are too sparse. This occurs even if the axisymmetric solutions appear to be well resolved. This suggests that different scaling factors should be used for the axisymmetric and eigenvalue problems. However, errors introduced in interpolation seem to negate the potential benefit of using different scaling factors. In the calculations presented, the scaling factor $\eta = 6$ is used. This is the smallest value that leads to qualitatively good results for the axisymmetric problem when $N = 20$; for smaller values of $\eta$, the boundary layer is not resolved well enough. Also, for larger values of $\eta$ (for $N = 20$), there is an insufficient number of interior points to adequately describe the eigenfunctions. However, for larger values of $N$, the results are consistent and not as sensitive to the choice of $\eta$.

**5.2. Solution techniques.** For the computation of the axisymmetric solution we use Newton's method. This method can be combined with a predictor-corrector continuation technique to find the axisymmetric solution for a wide range of parameter values. If $\Omega = 0$ and $\Delta T = 0$, then the trivial solution satisfies the axisymmetric equations. Thus for $\Omega$ and $\Delta T$ small, the trivial solution is a reasonable prediction of the solution, and Newton's method is used for the correction. For small increments in the parameter values, the previous solution is a reasonable prediction. To make larger increments in the parameter values, a secant line approximation can be used for the prediction.

Each point on a neutral stability curve is found using an iterative secant method, where the real part of the eigenvalue with largest real part is considered as a function of the parameters. The iterative procedure for the localization of the double Hopf points uses the fact that the points occur at intersections of two neutral stability curves. In both procedures, iteration continues until the magnitudes of the real parts of the relevant eigenvalues are less than a specified tolerance ($10^{-8}$ for the results presented below).

The discretized transformed equations and the entries of the coefficient matrices are computed symbolically using Maple. The generalized matrix eigenvalue problem, which results from the discretization of (4.6), is solved in Matlab using the implicitly restarted Arnoldi method [17], which is a memory-efficient iterative method for finding a specified number of eigenvalues with the largest magnitudes. A generalized Cayley transformation is made so that the Arnoldi iteration finds the eigenvalues with largest real parts [8]. The parameters of the transformation can also be chosen to improve convergence properties. In particular, the generalized Cayley transformation

$$\mathbf{C}(\mathbf{L},\mathbf{A}) = (\mathbf{L} - \alpha_1\mathbf{A})^{-1}(\mathbf{L} - \alpha_2\mathbf{A}) \tag{5.2}$$

maps eigenvalues $\lambda$ of the generalized matrix eigenvalue problem $\lambda\mathbf{A}v = \mathbf{L}v$ to eigenvalues $\sigma$ of the transformed matrix $\mathbf{C}(\mathbf{L},\mathbf{A})$, such that the eigenvalues $\lambda$ with $\mathrm{Real}(\lambda) > (\alpha_1 + \alpha_2)/2$ are mapped to the eigenvalues $\sigma$ with $|\sigma| > 1$, where $\alpha_1$ and $\alpha_2$ are the real parameters of the Cayley transformation. The matrix $\mathbf{C}(\mathbf{L},\mathbf{A})$ does not have to be formed explicitly, because the Arnoldi iteration only requires matrix-vector products involving $\mathbf{C}(\mathbf{L},\mathbf{A})$, see [17]. Thus, the full sparseness properties of $\mathbf{L}$ and $\mathbf{A}$ can be exploited, and computer memory requirements can be reduced.

**5.3. Convergence.** For the centered differencing that was used, the local truncation error is $O(h^2)$ (*i.e.* approximately a constant times $h^2$, as $h \to 0$), where $h$ is the mesh size. Given this and a few standard assumptions, the accuracy of the approximations for the boundary value problems will be $O(h^2)$. In addition, if the approximate solution and the differencing scheme for the derivative are both $O(h^2)$, then the approximations of derivatives of the solutions are also $O(h^2)$. However, for the present application, although the approximation of the partial differential eigenvalue problem by the matrix eigenvalue problem can be assumed to converge, the order of this convergence is unknown. Considering this, it is reasonable to assume that the approximations of the normal form coefficients converge, even though we could not say to what order.

An additional comment should be made concerning the eigenfunction approximation. It is obvious that a finite-dimensional approximation is not able to approximate all the solutions of the infinite-dimensional continuous eigenvalue problem. We expect that it is the highly oscillatory, high wave number eigenfunctions that the matrix problem is unable to resolve. Because the critical eigenfunctions of interest have relatively low wave numbers and are not highly oscillatory, we expect that these functions are resolved, and that the errors in the differencing are relatively small.

Our results, which are presented in the next section, indicate that the approximation of the normal form coefficients seem to be convergent. However, the mesh size $h$ could not be taken small enough to obtain an accurate estimate of the order of convergence.

Table 5.1

*The annulus geometry and fluid properties used in the analysis, after [4]. See text for definitions of symbols.*

| | | |
|---|---|---|
| $r_a$ | 3.48 | cm |
| $r_b$ | 6.02 | cm |
| $R$ | 2.54 | cm |
| $D$ | 5 | cm |
| $\nu$ | $1.01e^{-2}$ | $\mathrm{cm}^2/\mathrm{sec}$ |
| $\kappa$ | $1.41e^{-3}$ | $\mathrm{cm}^2/\mathrm{sec}$ |
| $\alpha$ | $2.06e^{-4}$ | $1/°$ C |
| $\rho_0$ | 0.998 | gm $\mathrm{cm}^3$ |
| $T_0$ | 20.0 | ° C |
| $g$ | 980 | $\mathrm{gm}/\mathrm{cm}^3$ |

**6. Results.** The results of our study are presented in this section. The parameter values specifying the geometry of the annulus and fluid properties are listed in Table 5.1. These values correspond to the experiments performed by Fein [4]. Our results are compared with those obtained in that study.

**6.1. The axisymmetric solution.** An example of the axisymmetric solution is plotted in Figure 6.1. Qualitatively, the form of the solution is the same for all values of the parameters. The figure shows that the fluid velocity in the interior of the fluid is predominantly in the azimuthal direction. The radial velocity is almost zero everywhere except near the upper and lower boundaries, where it is negative and positive, respectively. The vertical velocity is largest at the inner and outer walls, where there is rising at the warmer outer wall and sinking at the cooler inner wall. The interior azimuthal velocity exhibits an almost linear shear in the vertical, with a positive velocity in the upper half of the annulus and negative velocity in the lower half. The resulting circulation is a convection cell that is tilted from the radial plane such that, at the upper and lower boundaries, the inward and outward motion is deflected to the right. Although quantitative information of the experimental axisymmetric flow was not available, the computed flow profile qualitatively reproduces all the features of the experimental flow.

**6.2. Neutral stability and transition curves.** The neutral stability curves are presented in Figure 6.2. There is a separate curve for each azimuthal wave number. The curves consist of points in the parameter space where, for the given wave number, there is one pair of complex conjugate eigenvalues with zero real part while all other eigenvalues associated to that wave number have negative real part. Wave numbers from $m = 2$ to 10 were calculated and it was found that $m = 3$ to 8 were the only critical wave numbers. Therefore, only these are shown in Figure 6.2. It is not possible to calculate the neutral stability curves of all wave numbers, but it can be argued that the higher wave numbers will not be critical in the parameter range of interest. We refer the interested reader to [18] and here justify investigation of only a finite number of wave numbers by comparison with the experimental results. A $25 \times 25$ grid was used for the calculations of all curves shown.

In Figure 6.3, the curve that separates the axisymmetric regime from the non-axisymmetric regime is plotted. To the left of this curve, the axisymmetric solution is linearly stable (to perturbations of all wave numbers), while to the right, it is unstable. Along this curve it can be seen that there are transitions of the critical wave number. These transitions occur at intersections of the neutral stability curves and correspond to the double Hopf bifurcation points, *i.e.,* at these points there are two complex conjugate pairs of eigenvalues with zero real parts. Also plotted on Figure 6.3 is the experimentally observed transition curve taken from Fein [4], with critical wave number transitions. This is the curve where a transition from the axisymmetric to steady wave flow was observed. All curves are plotted on a log-log graph of the Taylor number $\mathcal{T}$ *versus* the thermal Rossby number $\mathcal{R}$ (see Section 2).

Linear analysis reproduces many of the experimental observations. By inspection of Figure 6.3, it can be seen that there is a good correspondence between the numerical and experimental transition curves. It has also been shown, via comparison with experimentally measured wave speeds at the transition, that the imaginary parts of the eigenvalues are also in agreement. See [19] for further discussion.

**6.3. Double Hopf normal form coefficients: hysteresis.** The numerical results are presented in Table 6.3. Included are the locations of the double Hopf

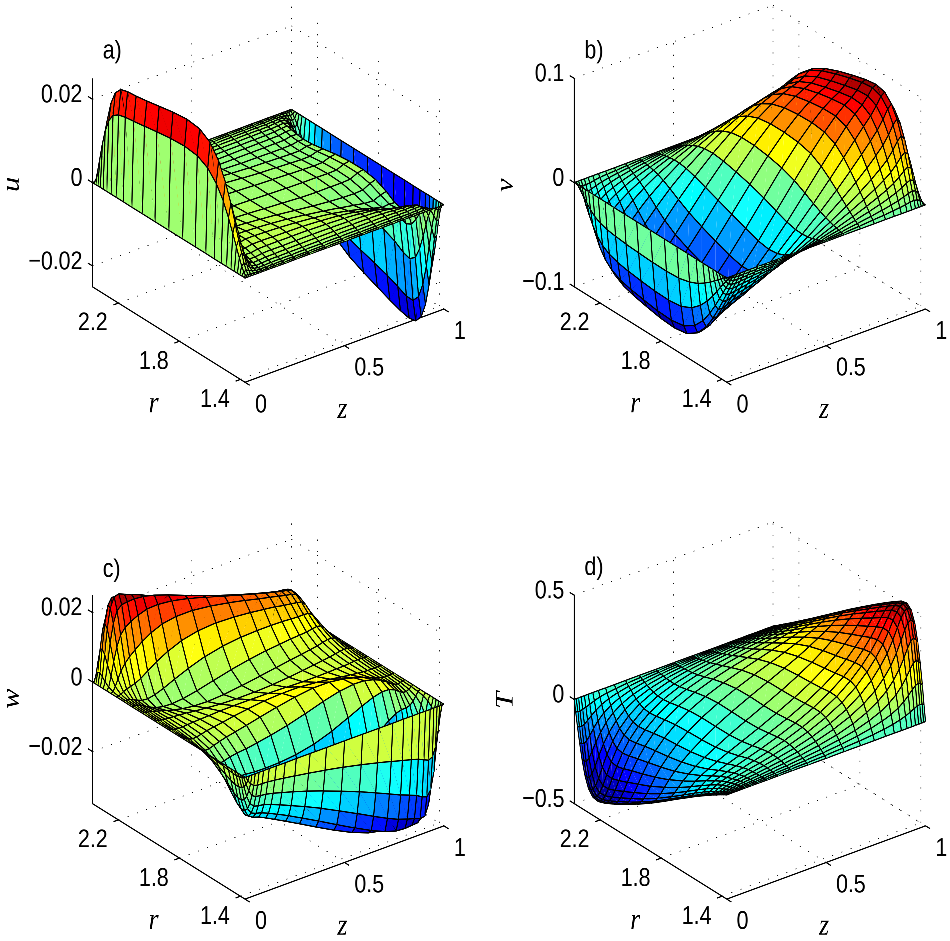

FIG. 6.1. *The axisymmetric solution: (a) $u$ the fluid velocity in the radial direction, (b) $v$ the fluid velocity in the azimuthal direction, (c) $w$ the fluid velocity in the vertical direction, and (d) $T$ the deviation of the temperature of the fluid from $\Delta T\,(r - r_a/R) + T_a$. This solution is for the $N = 25$ case and is observed at the $(m_1, m_2) = (6, 7)$ double Hopf point, where $\Omega = 0.5927$ and $\Delta T = 0.6950$.*

bifurcation points and the values of the normal form coefficients, as well as the values of the imaginary parts of the critical eigenvalues at the bifurcation point. The double Hopf points are labeled in terms of the associated critical wave numbers $m_1$ and $m_2$. For all double Hopf points, $a = -1$, $b < 0$, $c < 0$ and $d = -1$, and the condition $A = ad - bc < 0$ is also satisfied.

The dynamics are found from an investigation of the fixed points of the equations obtained by ignoring the $\theta_j$ in the normal form equations (4.20). To lowest order, the $\dot{\theta}_j$ equations add a constant rotation for each corresponding dimension. See [9] for a complete analysis of the normal form equations (4.20). Here, there are fixed points when

1. $\rho_1 = \rho_2 = 0$
2. $\rho_2 = 0$ and $\rho_1 = \rho_p = \sqrt{\dfrac{\mu_1}{-a}}$

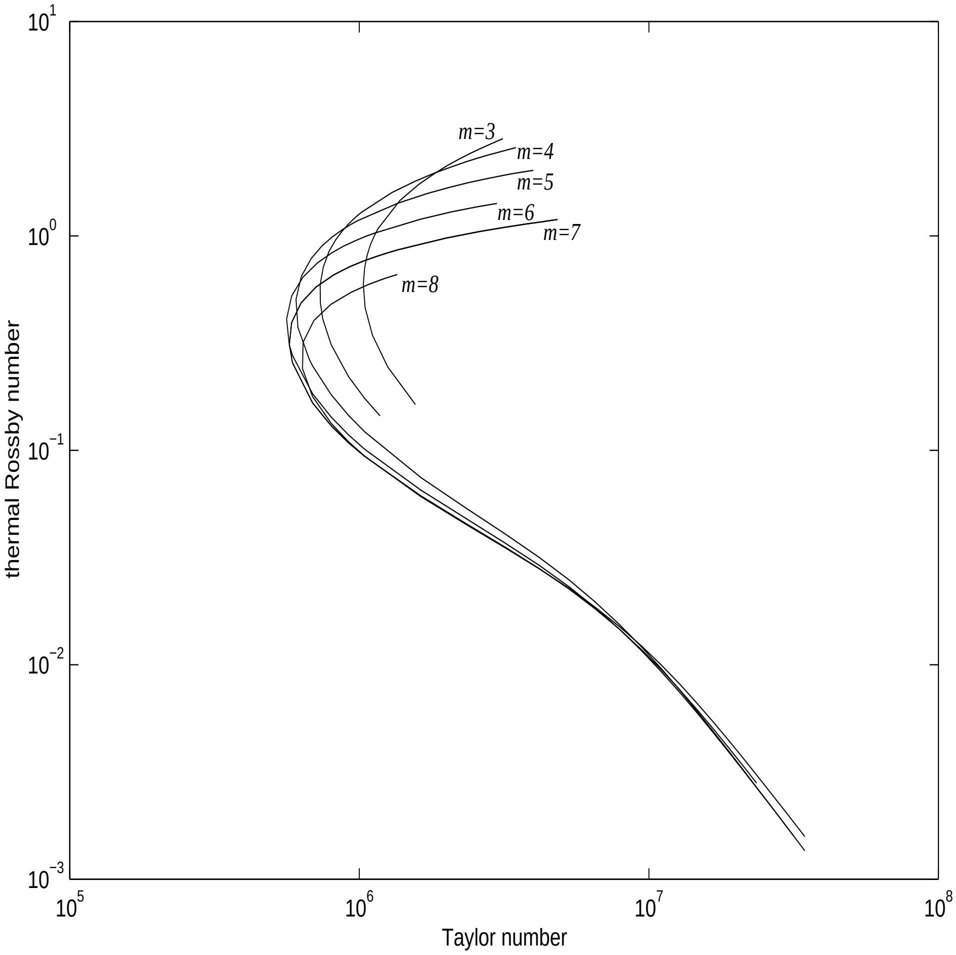

FIG. 6.2. *Neutral stability curves are plotted for the wave numbers $m = 3$ to $m = 8$. The curves are calculated by finding the parameter values where for each $m$, the eigenvalues of (4.6) all have negative real part except one with zero real part. The curves are plotted on a log-log graph of thermal Rossby number versus Taylor number.*

3. $\rho_1 = 0$ and $\rho_2 = \rho_q = \sqrt{\dfrac{\mu_2}{-d}}$
4. $\rho_1 = \rho_1^{(T)} = \sqrt{\dfrac{-d\mu_1 + b\mu_2}{A}}$ and $\rho_2 = \rho_2^{(T)} = \sqrt{\dfrac{c\mu_1 - a\mu_2}{A}}$

where $A = ad - bc$ and with the condition that the quantities inside the square root signs must be positive.

Fixed point (1) is a fixed point of the normal form equations for all values of the parameters. By inspection of the normal form equations (4.20), it is fairly easy to see that, regardless of the values of the coefficients, for small $\rho_1$ and $\rho_2$, $\dot{\rho}_1$ and $\dot{\rho}_2$ will have the same sign as $\mu_1$ and $\mu_2$, respectively. This means that solution (1) will be stable if both $\mu_1$ and $\mu_2$ are negative and unstable if either one is greater than zero. In the fluid annulus, this solution corresponds to the steady axisymmetric flow. Fixed points (2) and (3) correspond to periodic solutions of the normal form

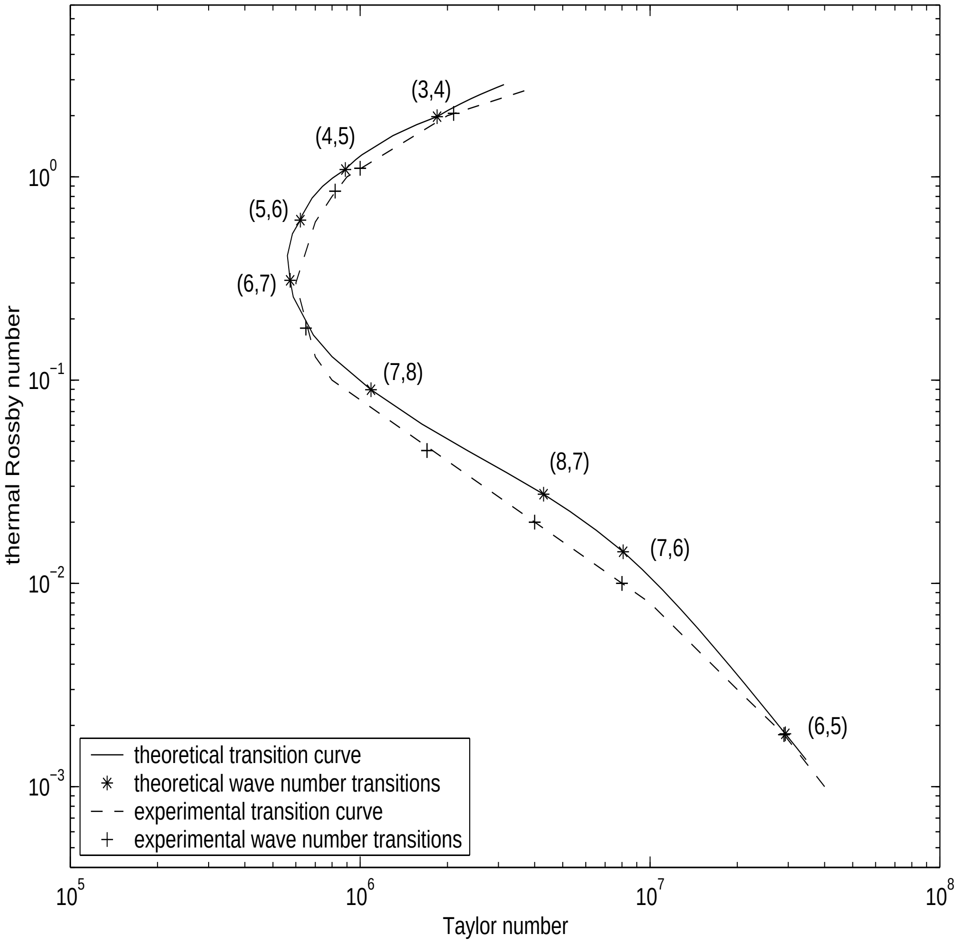

FIG. 6.3. *Transition curves for theory and experiment delineating the axisymmetric from the non-axisymmetric regimes. The critical wave number transitions (double Hopf bifurcation points), labelled as* $(m_1,\ m_2)$*, are also plotted along the curve.*

equations and exist when $\mu_1 > 0$ and $\mu_2 > 0$, respectively (because we have $a = -1$ and $d = -1$). In the fluid, these solutions correspond to non-axisymmetric, steadily rotating waves. The fixed point (4) corresponds to a 2-torus for the normal form equations and exists when $(-d\mu_1 + b\mu_2)/A > 0$ *and* $(c\mu_1 - a\mu_2)/A > 0$. Because we have $A < 0$, $a = -1$, $b < 0$, $c < 0$ and $d = -1$, the 2-torus exists in the wedge in $(\mu_1, \mu_2)$ parameter space given by $d\mu_1/b < \mu_2 < c\mu_1/a$, $\mu_1 > 0$, $\mu_2 > 0$. These solutions correspond to modulated wavy flow in the fluid.

TABLE 6.1

*Numerical results for double Hopf bifurcation points.* $a = -1$ *and* $d = -1$ *for all* $N$. $N$ *is number of grid points on one side,* $(\Omega_0, \Delta T_0)$ *is the location in parameter space where the bifurcation occurs,* $\omega_1$ *and* $\omega_2$ *are the imaginary parts of the eigenvalues at* $(\Omega_0, \Delta T_0)$ *and a,b,c and d are the normal form coefficients.*

| $N$ | $m_1$, $m_2$ | $\Omega_0$ | $\Delta T_0$ | $-\omega_1$ | $-\omega_2$ | $b$ | $c$ |
|---|---|---|---|---|---|---|---|
| 30 | 3, 4 | 1.025 | 12.76 | $2.320 \cdot 10^{-2}$ | $3.305 \cdot 10^{-2}$ | -1.0051 | -2.362 |
| 40 | 3, 4 | 1.030 | 12.93 | $2.514 \cdot 10^{-2}$ | $3.632 \cdot 10^{-2}$ | -0.9720 | -2.651 |
| 50 | 3, 4 | 1.034 | 13.04 | $2.560 \cdot 10^{-2}$ | $3.712 \cdot 10^{-2}$ | -0.9813 | -2.723 |
| 30 | 4, 5 | 0.7313 | 3.772 | $1.450 \cdot 10^{-2}$ | $1.936 \cdot 10^{-2}$ | -1.332 | -2.273 |
| 40 | 4, 5 | 0.7271 | 3.795 | $1.508 \cdot 10^{-2}$ | $2.018 \cdot 10^{-2}$ | -1.327 | -2.367 |
| 50 | 4, 5 | 0.7276 | 3.840 | $1.533 \cdot 10^{-2}$ | $2.053 \cdot 10^{-2}$ | -1.324 | -2.414 |
| 20 | 5, 6 | 0.6354 | 1.543 | $7.946 \cdot 10^{-3}$ | $1.039 \cdot 10^{-2}$ | -1.360 | -2.134 |
| 30 | 5, 6 | 0.6102 | 1.490 | $8.462 \cdot 10^{-3}$ | $1.091 \cdot 10^{-2}$ | -1.470 | -2.187 |
| 40 | 5, 6 | 0.6048 | 1.502 | $8.721 \cdot 10^{-3}$ | $1.124 \cdot 10^{-2}$ | -1.483 | -2.237 |
| 50 | 5, 6 | 0.6036 | 1.517 | $8.867 \cdot 10^{-3}$ | $1.141 \cdot 10^{-2}$ | -1.488 | -2.265 |
| 20 | 6, 7 | 0.6117 | 0.6972 | $3.711 \cdot 10^{-3}$ | $4.960 \cdot 10^{-3}$ | -1.473 | -2.253 |
| 30 | 6, 7 | 0.5838 | 0.6944 | $4.046 \cdot 10^{-3}$ | $5.398 \cdot 10^{-3}$ | -1.532 | -2.256 |
| 40 | 6, 7 | 0.5757 | 0.7008 | $4.217 \cdot 10^{-3}$ | $5.611 \cdot 10^{-3}$ | -1.556 | -2.269 |
| 50 | 6, 7 | 0.5727 | 0.7071 | $4.317 \cdot 10^{-3}$ | $5.735 \cdot 10^{-3}$ | -1.568 | -2.277 |
| 20 | 7, 8 | 0.8699 | 0.3959 | $8.582 \cdot 10^{-4}$ | $1.161 \cdot 10^{-3}$ | -1.628 | -2.433 |
| 30 | 7, 8 | 0.7925 | 0.3758 | $9.294 \cdot 10^{-4}$ | $1.283 \cdot 10^{-3}$ | -1.616 | -2.408 |
| 40 | 7, 8 | 0.7652 | 0.3713 | $9.750 \cdot 10^{-4}$ | $1.356 \cdot 10^{-3}$ | -1.625 | -2.404 |
| 50 | 7, 8 | 0.7505 | 0.3704 | $10.09 \cdot 10^{-4}$ | $1.410 \cdot 10^{-3}$ | -1.631 | -2.399 |
| 20 | 8, 7 | 1.603 | 0.4692 | $4.010 \cdot 10^{-4}$ | $3.493 \cdot 10^{-4}$ | -2.309 | -1.748 |
| 30 | 8, 7 | 1.635 | 0.4581 | $3.748 \cdot 10^{-4}$ | $3.284 \cdot 10^{-4}$ | -2.274 | -1.723 |
| 40 | 8, 7 | 1.655 | 0.4559 | $3.602 \cdot 10^{-4}$ | $3.156 \cdot 10^{-4}$ | -2.270 | -1.722 |
| 50 | 8, 7 | 1.670 | 0.4556 | $3.501 \cdot 10^{-4}$ | $3.064 \cdot 10^{-4}$ | -2.268 | -1.722 |
| 20 | 7, 6 | 2.226 | 0.4625 | $1.5529 \cdot 10^{-4}$ | $1.3613 \cdot 10^{-4}$ | -2.311 | -1.734 |
| 30 | 7, 6 | 2.231 | 0.4457 | $1.4406 \cdot 10^{-4}$ | $1.2289 \cdot 10^{-4}$ | -2.309 | -1.719 |
| 40 | 7, 6 | 2.250 | 0.4391 | $1.3228 \cdot 10^{-4}$ | $1.1086 \cdot 10^{-4}$ | -2.310 | -1.718 |
| 50 | 7, 6 | 2.269 | 0.4356 | $1.2318 \cdot 10^{-4}$ | $1.0177 \cdot 10^{-4}$ | -2.310 | -1.717 |
| 20 | 6, 5 | 3.843 | 0.2559 | $2.064 \cdot 10^{-5}$ | $2.083 \cdot 10^{-5}$ | -2.376 | -1.746 |
| 30 | 6, 5 | 4.696 | 0.1718 | $2.278 \cdot 10^{-5}$ | $2.198 \cdot 10^{-5}$ | -2.350 | -1.733 |
| 40 | 6, 5 | 5.886 | 0.1148 | $2.257 \cdot 10^{-5}$ | $2.165 \cdot 10^{-5}$ | -2.336 | -1.729 |
| 50 | 6, 5 | 7.449 | 0.0764 | $2.315 \cdot 10^{-5}$ | $2.220 \cdot 10^{-5}$ | -2.330 | -1.730 |

A linear stability analysis of fixed points (2), (3) and (4) gives the local behaviour near the bifurcation points. See Figure 6.4 for the bifurcation diagram. The results indicate that both of the bifurcating waves, corresponding to the fixed points (2) and (3), are stable in the wedge where the 2-torus exists. Thus, the boundaries of the wedge $\mu_2 = d\mu_1/b$ and $\mu_2 = c\mu_1/a$ give the boundaries of the region of bistability of the wave solutions. Furthermore, because only one of the bifurcating waves loses stability on each of the boundaries of the wedge, there is hysteresis. The results also indicate that the 2-torus is always unstable. In Figure 6.6, the approximate boundaries of the region of bistability are drawn. The bifurcation diagram in Figure 6.5 shows the hysteresis that occurs when a one-parameter path through the parameter space crosses the region of bistability. The parameter $s$ could be either $\Omega$ or $\Delta T$ or a function of both, depending on particular circumstances. An example of such a path is indicated on Figure 6.4.

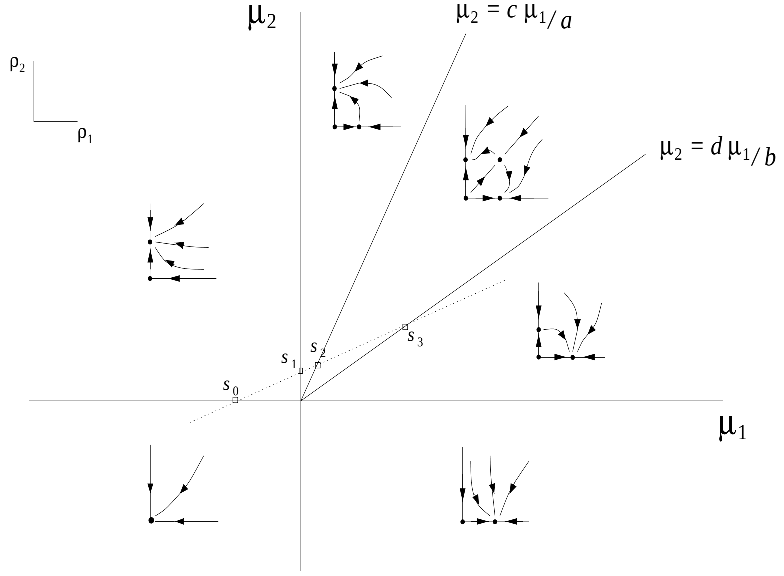

FIG. 6.4. *The two-dimensional bifurcation diagram. The diagram is displayed using the real parts of the critical eigenvalues $\mu_1$, $\mu_2$ as the bifurcation parameters. The regions of different character are separated by solid lines. In each region, the corresponding phase portrait is drawn, where the phase portraits are presented in $\rho_1$, $\rho_2$ coordinates. The $\theta_1$ and $\theta_2$ equations in (4.20) add a constant rotation to each coordinate. The dotted line indicates a possible one-parameter path which will lead to hysteresis. The bifurcation points along this path are indicated by $s_0$, $s_1$, $s_2$ and $s_3$ (see Figure 6.5).*

Quantitative verification of the predicted hysteresis is not currently possible due to the lack of available experimental data for the specific annulus studied here. Furthermore, although the extent of hysteresis has been mapped for other transitions in other regions of parameter space (see *e.g.* [5], [14], [16], and [4]), there is relatively little data concerning the hysteresis that occurs in the transitions between steady waves near the axisymmetric regime. Also, many experimental results in the steady wave regime are quoted in terms of the wave number that is most likely to occur. Our analysis cannot predict this.

Concerning the convergence of the numerical approximations, it can be seen that the numerical differences between the normal form coefficients at the different levels

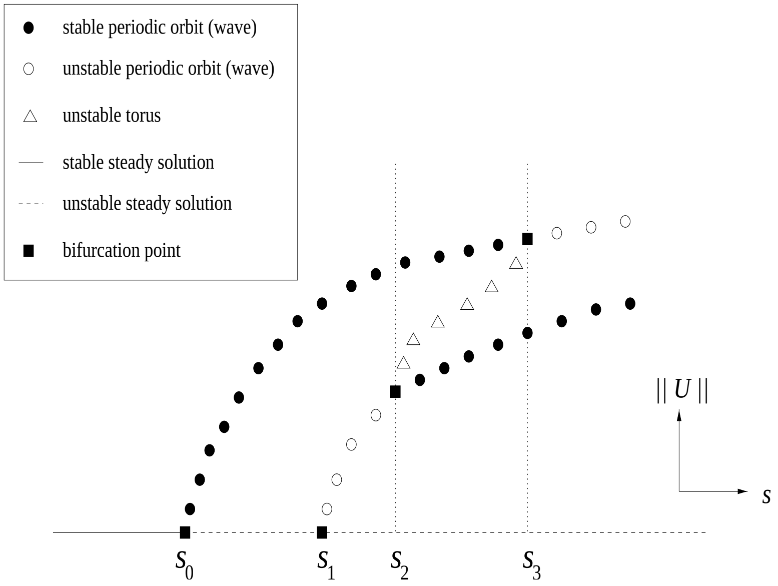

FIG. 6.5. *The one-dimensional bifurcation diagram depicting the bifurcation observed along the path indicated with the dotted line in Figure 6.4. The bifurcation points are labelled as $s_0$, $s_1$, $s_2$ and $s_3$. $||U||$ is a measure of the size of the solution and $s$ is the bifurcation parameter.*

of discretization decrease with increasing discretization level (see Table 6.3). This is an indication of convergence. However, it appears that $N$ is not large enough to make an estimation of the order of convergence. Yet, the differences in the normal form coefficients at different $N$ are quite small, which is evidence that these results are at least qualitatively accurate. To say this with more certainty, the analysis must be performed using higher levels of discretization. This was not possible with the available resources. Because the results accurately reproduce the experimental results, we conclude that the approximations are satisfactory.

The results for the $(m_1, m_2) = (3, 4)$ and $(m_1, m_2) = (4, 5)$ double Hopf points are not complete (see Table 6.3). For these wave number pairs with $N = 20$, the eigenfunctions are not well resolved, and the eigenvalues are inaccurate. Also, the evidence of convergence of the normal form coefficients (see Table 6.3) is weaker for the double Hopf points at higher differential heating. It seems that the increase in numerical difficulty is not caused by the difficulty of resolving the boundary layer in the axisymmetric solution, but rather by the difficultly of resolving the eigenfunctions in the interior of the domain.

**6.4. The eigenfunctions: bifurcating wave form .** An example of an eigenfunction is plotted in Figure 6.7. This is the eigenfunction with wave number $m = 6$ that is observed at the $(m_1, m_2) = (6, 7)$ double Hopf point (see Table 6.3). From equation (4.20), the periodic orbit corresponding to the wave with wave number $m_1$, to lowest order in $\mu_1$, is given by

$$\begin{aligned} \rho_1 &= \sqrt{\frac{-\mu_1}{a}} + O(\mu_1), \\ \theta_1 &= \omega_1 t + O(\mu_1), \end{aligned} \tag{6.1}$$

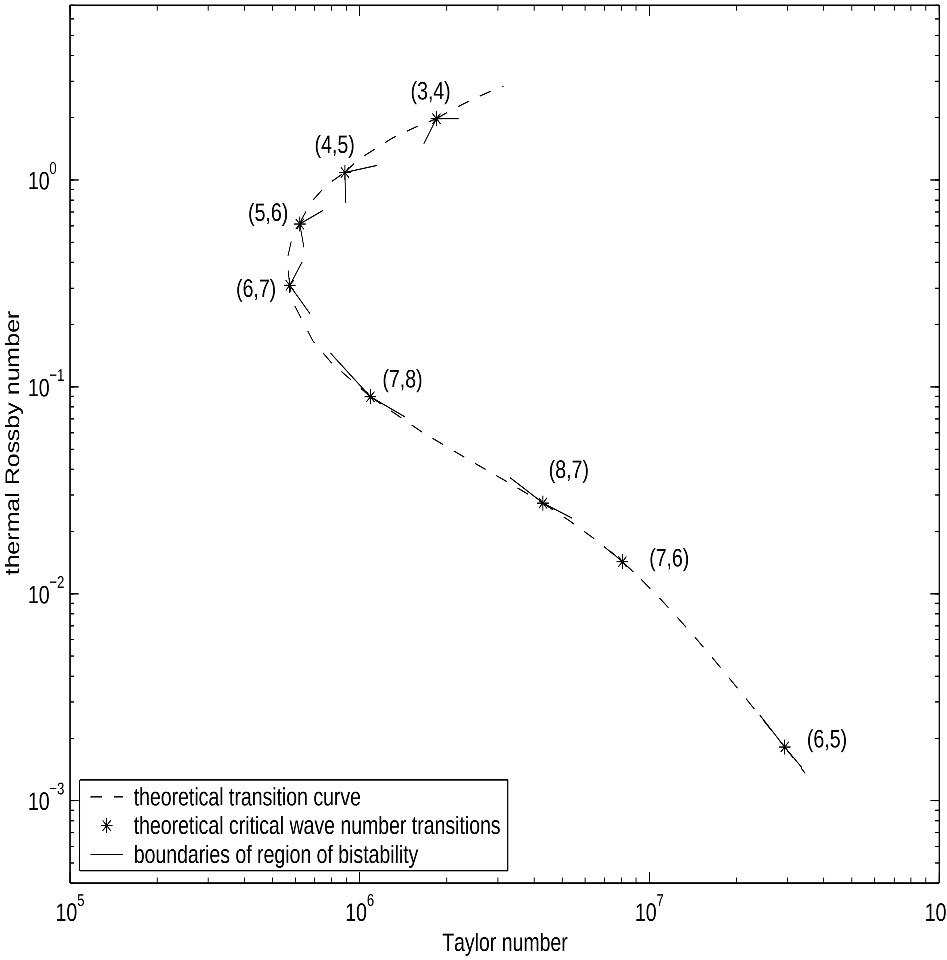

FIG. 6.6. *Theoretical transition curve between the axisymmetric and the non-axisymmetric regimes including the boundaries of the region of bistability. The boundaries are the solid lines attached to the double Hopf points. For each double Hopf point, the area between the boundaries is the region where there is bistability of wave solutions.*

or in terms of $z_1$,

$$z_1 = \sqrt{\frac{-\mu_1}{a}} e^{i\omega_1 t} + O(\mu_1), \tag{6.2}$$

which describes a near-circular periodic orbit. The periodic orbit corresponding to the wave with wave number $m_2$ is given by a similar expression. In terms of the variables of the perturbation equations (4.2)–(4.4), to lowest order, the periodic solution correspoding to (6.1) is given by $U = [\mathbf{u}, T] = z_1\Phi_1 + \overline{z}_1\overline{\Phi}_1 = \mathrm{Re}\,(z_1\Phi_1)$. That is,

$$\begin{aligned} U &= \mathrm{Re}\left[\sqrt{\frac{-\mu_1}{a}} e^{i\omega_1 t}\tilde{\Phi}_{m_1} e^{im_1\varphi}\right] + O(\mu_1) \\ &= \sqrt{\frac{-\mu_1}{a}}\left[\tilde{\Phi}^r_{m_1}\cos(m_1\varphi + \omega_1 t) - \tilde{\Phi}^i_{m_1}\sin(m_1\varphi + \omega_1 t)\right] + O(\mu_1), \end{aligned} \tag{6.3}$$

*i.e.* a rotating wave, where $\Phi_1 = \tilde{\Phi}_{m_1} e^{im_1\varphi}$, and where $\tilde{\Phi}^r_{m_1}$ and $\tilde{\Phi}^i_{m_1}$ denote the real and imaginary parts of $\tilde{\Phi}_{m_1}$. In terms of the variables of the original equations (3.5)–(3.7), the solution $U$ corresponds to deviations from the axisymmetric solution $\left[\mathbf{u}^{(0)}, T^{(0)}\right]$ of the same equations. Also, if $t$ is fixed, then at different $\varphi$, the periodic solution is a different linear combination of $\tilde{\Phi}^r_{m_1}$ and $\tilde{\Phi}^i_{m_1}$, and so, the form of the eigenfunction gives the form of the bifurcating wave, to the lowest order of approximation. That is, the approximation is valid for parameter values that are close to the axisymmetric-to-wave transition curve.

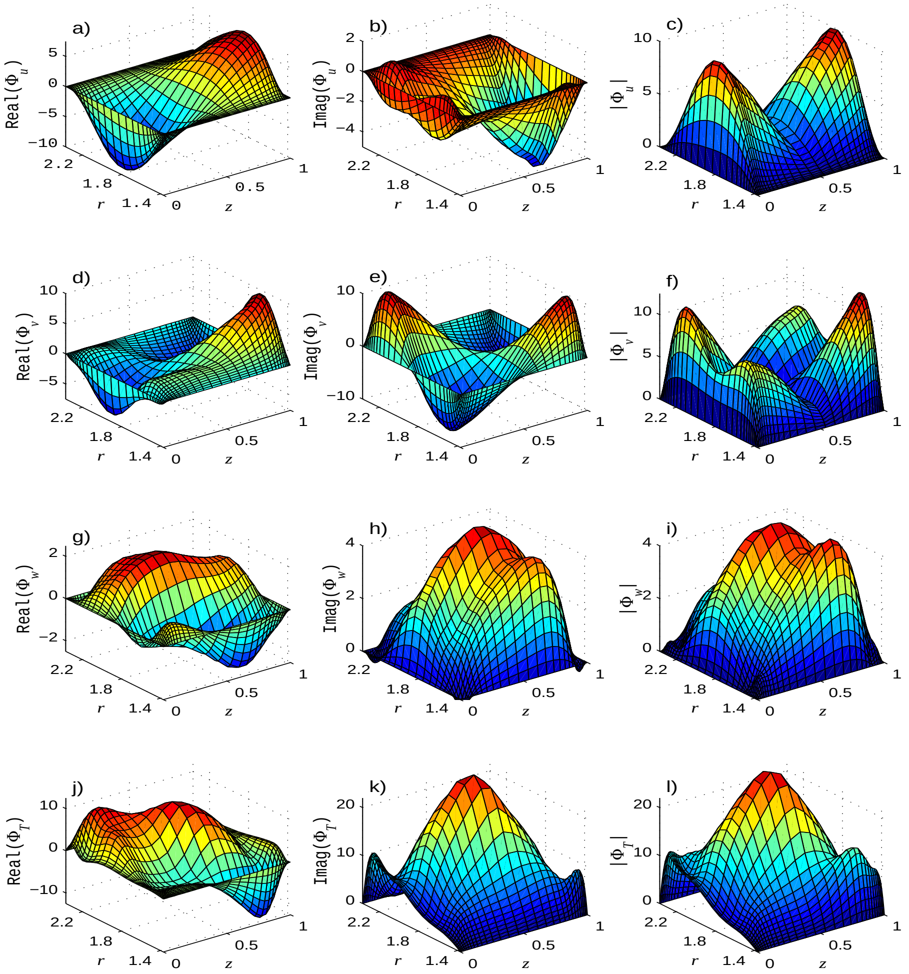

FIG. 6.7. *An example of the radial and vertical dependence of an eigenfunction with* $m = 6$ *and* $N{=}30$ *at* $\Omega = 0.5838$ *and* $\Delta T = 0.6944$*: (a) real part, (b) imaginary part, and (c) amplitude of the radial component of the eigenfunction, (d) real part, (e) imaginary part, and (f) amplitude of the azimuthal component of the eigenfunction, (g) real part, (h) imaginary part, and (i) amplitude of the vertical component of the eigenfunction, (j) real part, (k) imaginary part, and (l) amplitude of the temperature component of the eigenfunction. That is, the actual components of the eigenfunctions are the plotted functions multiplied by* $e^{im\varphi}$.

The form of the bifurcating wave is consistent with previous results. Measurements, from experiments with the same annulus geometry as is used for our results, indicate that the temperature has a maximum at mid-radius mid-depth [4]. Furthermore, the coarse features of the wave form are consistent with the detailed experimental and numerical results of [15], as well as the numerical results of [27], even though different annulus geometries, waves with different dominant wave numbers, and waves far from the axisymmetric-to-wave transition curve, are studied. This includes (see Figures 5 and 6 of [15]) the radial dependence of the Fourier amplitude of the dominant wave number of the radial velocity at various heights, and the radial dependence of the Fourier amplitude of the dominant wave number of the azimuthal velocity at mid-depth. In our case, the square of the Fourier amplitude is given by $\left(\tilde{\Phi}^r_{m_j}\right)^2 + \left(\tilde{\Phi}^i_{m_j}\right)^2$. See also Figure 8 in [27] for the vertical dependence of the deviations from the azimuthally averaged flow of both temperature and velocity for the (numerical) wave forms in an annulus without a rigid lid. However, compared to our bifurcating waves (6.3), the waves of these experimental and numerical studies show a relative decrease in the amplitude at mid-radius of the azimuthal average of the azimuthal velocity (*i.e.* the wave number zero Fourier component of the azimuthal velocity). In our case, the azimuthal average to first order is given by the axisymmetric solution $\left[\mathbf{u}^{(0)}, p^{(0)}, T^{(0)}\right]$ (see Figure 6.1). The waves studied in [15] and [27] are observed in regions of parameter space far from the axisymmetric-to-wave transitions, where the higher-order terms in (6.3), which we have ignored, may be important. Although these higher-order terms do not produce a significant qualitative change in the deviations from the azimuthally averaged flow, they do seem to produce a small, but noticeable, qualitative difference on the the azimuthal averaged flow itself. In order to study this effect, the bifurcating waves (6.3) would have to be calculated for parameter values far from the transition curve.

**7. Conclusion.** In this paper, we study the transitions from axisymmetric steady solutions to non-axisym-metric waves in a Navier-Stokes model of the differentially heated rotating annulus experiment. An analytical–numerical center manifold reduction is used to analyze the double Hopf bifurcation points that occur at this transition. The results, that are obtained by numerically approximating the coefficients of the normal form equations, show that there are stable waves that bifurcate from the axisymmetric solution *via* a Hopf bifurcation, and that hysteresis of the bifurcating waves occurs near critical wave number transitions. Associated with the hysteresis is the existence of an unstable torus. Approximate boundaries to the region of bistability are drawn. The results are consistent with laboratory experiments, which supports not only the validity of the model, but also the validity of the analysis. Although the convergence of the numerical approximations cannot be proven, the evidence of convergence and the correspondence with experimental results supports the claim that the behaviour, that is predicted by our results, occurs in the full partial differential equation model.

The behaviour seen in the model of the experiment is qualitatively the same as that seen in the models of the analytical studies discussed in the first section. This is very interesting because the models of these analytical studies are simplified models of atmospheric circulation, and so they are of a very different scale from that of the experiment. That is, the method of analysis is able to highlight the dynamical similarity of two geophysical fluid models of vastly different scales. The similarity is evidence for the usefulness of studying the models of both scales and that both types of models incorporate the fundamental properties of differentially heated rotating systems.

The study presented here is a beginning, and there are many possible directions future work could take. The models of atmospheric circulation of the analytical studies, mentioned above, are quite simplified. The success of the numerical computations of the present study gives confidence that analysis of this type could be applied to more realistic atmospheric models, such as that presented in [3]. Also, in the analysis of the annulus experiment, there is the possibility of resonant behaviour close to an experimentally observed 'triple-point', which is a point in parameter space that is shared by three regimes (the axisymmetric, the wave and the irregular regimes; see Figure 2.2). The $(m_1, m_2) = (6, 5)$ double Hopf point, which occurs in a similar region in parameter space as the experimentally observed triple-point, is close to being resonant, *i.e.* the imaginary parts of the two complex conjugate pairs of eigenvalues with largest real part are nearly equal. Thus, a strongly resonant double Hopf bifurcation might be found by varying a third parameter, and in this case, the dynamics found close to the resonant bifurcation may explain the existence of the triple-point.

Another interesting direction would be to attempt to follow the bifurcating solutions as the parameters move away from the bifurcation point. Two interesting flows that are observed in the annulus (both experimentally and numerically) are amplitude vacillation and wave dispersion [14], [22]. It has been hypothesized that the mechanism responsible for both of these flows is an interaction of two waves *via* a stable torus, where amplitude vacillation results from an interaction of two waves of the same dominant azimuthal wave number, while wave dispersion results from an interaction of waves with different dominant azimuthal wave numbers ([23], [21]; see also [5] for experimental evidence).

The unstable torus, that we have shown to exist in the steady wave regime, is such an interaction of two waves with different wave numbers. Thus, it is possible that if the unstable torus could be followed further into the steady wave regime, a bifurcation to a stable torus (and wave dispersion) may be discovered. Alternatively, if the stable periodic orbits corresponding to the wave solutions could be followed further into the wave regime, a bifurcation to a stable torus might occur, which may result in the discovery of either amplitude vacillation or wave dispersion. At the moment, such a study seems computationally prohibitive. However, if the curvature of the annulus is neglected, a symmetry of the resulting system leads to a bifurcation to a steady solution as opposed to a periodic orbit. In this case, the computation may be possible.

The comparison of theoretical and experimental results that took place in the investigation of the Taylor-Couette flow led to many more discoveries about the system than otherwise would have occurred. The work presented here begins such a comparison for the differentially heated rotating annulus flow. Some of our results are confirmed by comparison with experiments, and some predictions, concerning the boundaries of the region of bistability, have yet to be verified. For future work, we expect that the use of such techniques will lead to further discovery of new dynamics, both theoretical and experimental, which in turn will lead to a better general understanding of differentially heated rotating fluid systems.

## REFERENCES

[1] P. CHOSSAT AND G. IOOSS, *The Couette-Taylor Problem*, vol. 102 of Applied Mathematical Sciences, Springer-Verlag, New York, 1994.

[2] P. Drazin, *Nonlinear baroclinic instability of a continuous zonal flow of viscous fluid*, Journal of Fluid Mechanics, 55 (1972), pp. 577–587.

[3] J. Dutton and P. Kloeden, *The existence of Hadley convective regimes of atmospheric motion*, Journal of the Australian Mathematical Society, Series B, 24 (1983), pp. 318–338.

[4] J. Fein, *An experimental study of the effects of the upper boundary condition on the thermal convection in a rotating cylindrical annulus of water*, Geophysical Fluid Dynamics, 5 (1973), pp. 213–248.

[5] W.-G. Früh and P. Read, *Wave interactions and the transition to chaos of baroclinic waves in a thermally driven rotating annulus*, Philosophical Transactions of the Royal Society of London, A, 355 (1997), pp. 101–153.

[6] M. Ghil and P. Childress, *Topics in Geophysical Fluid Dynamics*, vol. 60 of Applied Mathematical Sciences, Springer-Verlag, 1987.

[7] J. Gierling and R. Eckhard, *Double Hopf bifurcation and interaction of Rossby-waves induced by the zonal flow*, Contributions in Atmospheric Physics, 71 (1998), pp. 427–444.

[8] W. Govaerts, *Numerical Methods for Bifurcations of Dynamical Equilibria*, SIAM, Philadelphia, 2000.

[9] J. Guckenheimer and P. Holmes, *Nonlinear Oscillations, Dynamical Systems and Bifurcations of Vector Fields*, vol. 42 of Applied Mathematical Sciences, Springer-Verlag, New York, 1983.

[10] J. Hart, *Wavenumber selection in nonlinear baroclinic instability*, Journal of the Atmospheric Sciences, 38 (1984), pp. 400–408.

[11] B. Hassard, N. Kazarinoff, and Y.-H. Wan, *Theory and Applications of Hopf Bifurcation*, vol. 41 of London Mathematical Society Lecture Note Series, Cambridge University Press, 1981.

[12] D. Henry, *Geometric Theory of Semilinear Parabolic Equations*, vol. 840 of Lecture Notes in Mathematics, Springer-Verlag, Berlin, 1981.

[13] R. Hide and J. Mason, *Sloping convection in a rotating fluid*, Advances in Geophysics, 24 (1975), pp. 47–100.

[14] P. Hignett, *Characteristics of amplitude vacillation in a differentially heated rotating fluid annulus*, Geophysical and Astrophysical Fluid Dynamics, 31 (1985), pp. 247–281.

[15] P. Hignett, A. White, R. Carter, W. Jackson, and R. Small, *A comparison of laboratory measurements and numerical simulations of baroclinic wave flows in a rotating cylindrical annulus*, Quarterly Journal of the Royal Meteorological Society, 111 (1985), pp. 131–154.

[16] E. Koschmieder and H. White, *Convection in a rotating, laterally heated annulus: the wave number transitions*, Geophysical and Astrophysical Fluid Dynamics, 18 (1981), pp. 279–299.

[17] R. Lehoucq, D. Sorensen, and C. Yang, *ARPACK Users' Guide: Solution of Large-Scale Eigenvalue Problems with Implicitly Restarted Arnoldi Methods*, SIAM, Philadelphia, 1998.

[18] G. Lewis, *Double Hopf Bifurcations in Two Geophysical Fluid Dynamics Models*, PhD thesis, University of British Columbia, 2000.

[19] G. Lewis and W. Nagata, *Linear stability analysis for the differentially heated rotating annulus*. Submitted to *Geophysical and Astrophysical Fluid Dynamics*.

[20] J. Mansbridge, *Wavenumber transition in baroclinically unstable flows*, Journal of the Atmospheric Sciences, 41 (1984), pp. 925–930.

[21] I. Moroz and P. Holmes, *Double Hopf bifurcation and quasi-periodic flow in a model for baroclinic instability*, Journal of the Atmospheric Sciences, 41 (1984), pp. 3147–3160.

[22] R. Pfeffer and W. Fowlis, *Wave dispersion in a rotating, differentially heated cylindrical annulus of fluid*, Journal of the Atmospheric Sciences, 25 (1968), pp. 361–371.

[23] D. Rand, *Dynamics and symmetry. Predictions for modulated waves in rotating fluids*, Archive for Rational Mechanics and Analysis, 79 (1982), pp. 1–37.

[24] D. Tritton, *Physical Fluid Dynamics*, Oxford University Press, Oxford, UK., 1988.

[25] W. Weimer and H. Haken, *Chaotic behavior and subcritical formation of flow patterns of baroclinic waves for finite dissipation*, Journal of the Atmospheric Sciences, 46 (1989), pp. 1207–1218.

[26] S. Wiggins, *Introduction to Applied Nonlinear Dynamical Systems and Chaos*, vol. 2 of Texts in Applied Mathematics, Springer-Verlag, New York, 1990.

[27] G. Williams, *Baroclinic annulus waves*, Journal of Fluid Mechanics, 49 (1971), pp. 417–449.